2011

Relaxation imaging to characterize lightweight polymer-crosslinked aerogels

Emmalou T. Satterfield
Missouri University of Science and Technology, emma@mst.edu

Department:

RELAXATION IMAGING TO CHARACTERIZE LIGHTWEIGHT POLYMER-CROSSLINKED AEROGELS

by

EMMALOU THERESA SATTERFIELD

A THESIS

Presented to the Faculty of the Graduate School of the

MISSOURI UNIVERSITY OF SCIENCE AND TECHNOLOGY

In Partial Fulfillment of the Requirements for the Degree

MASTER OF SCIENCE IN CHEMISTRY

2011

Approved by

Klaus Woelk, Advisor
Thomas P. Schuman
Yangchuan Xing

ABSTRACT

Silica aerogels are three-dimensional assemblies of silica nanoparticles with extremely low densities. In some instances, the internal void volume is more than 90% of the total volume. The highly porous structure of the aerogels leads to attractive properties for thermal and noise insulation, due to very low thermal conductivity and very high acoustic impedance. The strength of silica aerogels has been substantially improved by casting a thin conformal polymer coating over the entire internal porous surfaces of the nanostructure. The coating reinforces the interparticle connections without significantly compromising the internal void space.

To analyze and compare the properties of several lightweight polymer-crosslinked silica aerogels, spatially resolved T_1 and T_2 relaxation studies were conducted. The polymer-crosslinked aerogels were precision-machined to snugly fit into the lower parts of standard NMR tubes. A mixture of equal amounts of acetone and deuterated acetone was used as the liquid to fill the void volume of the aerogels. Spin-echo and saturation-recovery relaxation sequences were used as part of a standard one-dimensional gradient-recalled echo imaging sequence. For comparison, native aerogels without the polymer coating were examined with the same pulse sequences. Because of the fragile nanoparticle network, native gels could not be machined but were generated directly inside the NMR tubes. The porosity of the gels was determined using the relaxation profiles. The relaxation times were found to have a significant dependence on the coating polymer and also on the formation process of the aerogels. In addition, the relationship between the pore size and relaxation time was also analyzed.

ACKNOWLEDGMENTS

I would first like to extend my deepest and sincere gratitude to my advisor, Dr. Klaus Woelk, for his years of guidance and support, both in my research experience and personal development. His constant support and patience have been a great source of inspiration for me. I would also like to thank Dr. Thomas Schuman and Dr. Yangchuan Xing for serving on my committee.

I would like to acknowledge the facilities and financial support provided by the Chemistry Department at the Missouri University of Science and Technology, as well as the financial support of the NSF-CHE 0943442 Grant. I would also like to thank Dr. Chariklia Sotiriou-Leventis, Dr. Nicholas Leventis, and Sudhir Mulik for providing the aerogel samples and the corresponding BET measurments and bulk densities.

I would also like to thank Wenjia Zhang for assistance on this project in addition to her valued friendship throughout my studies. I would like to acknowledge Megan Oldroyd for her assistance on this project. Special thanks to Dr. Rex Gerald for always encouraging me and trying to help me find ways to improve.

I would like to thank my family and friends: my wonderful parents, Franklin and Adele Schmittzehe, my brother and sisters, Josh, Katie, Evonne, and Jackie, and my other mother, Annie. Without their support and encouragement I would not have finished this. And last but not least, I would like to convey my gratitude to my loving husband, JR Satterfield, who supports me unendingly.

TABLE OF CONTENTS

LIST OF ILLUSTRATIONS

LIST OF TABLES

1. INTRODUCTION

1.1. NMR

Nuclear magnetic resonance (NMR) is a spectroscopic technique that utilizes the magnetic property of nuclei to analyze compounds. Nuclei that possess a magnetic moment can be studied using NMR [1, 2, 3]. The nuclear magnetic moment, μ, is a result of the intrinsic angular momentum of the nucleus, *P*. The nuclear magnetic moment and angular momentum are proportional to one another, as indicated by Equation 1. The proportionality factor, γ, is called the magnetogyric ratio and is specific to the nuclide being studied.

$$\mu = \gamma P \tag{1}$$

The angular momentum of a nucleus is quantized and can be determined from the angular momentum quantum number, *I*, which is also known as the nuclear spin. Equation 2 illustrates the relationship between the nuclear angular momentum and the nuclear spin, where $\hbar = h/2\pi$ and *h* is Planck's constant. Nuclear spin is due to unpaired protons and neutrons in the nucleus of an atom; it is known to have half-integer values up to 6, thus values of nuclear spin can be 0, ½, 1, 1 ½, etc. A nucleus with a nuclear spin of zero has no magnetic moment and cannot be observed using NMR.

$$P = \sqrt{I(I+1)}\,\hbar \tag{2}$$

When no external magnetic field is present the nuclear magnetic moments, commonly referred to as spins, are randomly oriented. These spins all have the same energy and occupy the same energy level. When the nuclei are introduced to an external magnetic field the spins align in a finite number of orientations relative to the applied field. Each of these orientations corresponds to a different energy level. The number of possible orientations is determined by the magnetic quantum number. The magnetic quantum number is related to the nuclear spin, having values from *I* to -*I* (e.g. $m_I = I, I - 1, \ldots, -I$). Therefore, nuclei with a nuclear spin of ½ the spins can have two possible

orientations, ½ and -½; for larger values of nuclear spin there are more possible orientations. Nuclides such as ^{1}H and ^{13}C are commonly studied using NMR and have a nuclear spin of ½. When introduced to an external magnetic field, these spins align either in the direction of the field or against the field and precess about the magnetic field [1, 2, 3, 4]. The frequency of this precession, called the Larmor frequency, is proportional to the applied magnetic field. Equation 4 illustrates the relationship between the applied magnetic field, B_0, and the Larmor frequency, ν_L, of a specific nuclide.

$$\nu_L = \frac{\gamma B_0}{2\pi} \tag{4}$$

The ratio of the number of spins in the upper energy level, N_β, to the number of spins in the lower energy level, N_α, is described by Boltzmann statistics [1, 5] as shown in Equation 5, where k is the Boltzmann constant. The ratio of spins is dependent on the difference in energy between upper and lower energy levels, ΔE, and the absolute temperature, T.

$$\frac{N_\beta}{N_\alpha} = \exp\left(-\frac{\Delta E}{kT}\right) \tag{5}$$

At room temperature the levels have near equal spin populations with a small excess in the lower energy state, corresponding to the alignment along the direction of the applied magnetic field. This population difference results in a net magnetic moment along the applied magnetic field, also referred to as net magnetization. Figure 1.1 shows a classical representation of the nuclear spins for spin ½ nuclides in the presence of an applied magnetic field and the resulting net magnetic moment. The energy level separation in combination with the population difference makes it possible to study molecules with NMR.

NMR is generally used for structural analysis of organic compounds [1, 6]. A simple one pulse experiment can be used to yield structural information; in this type of experiment the sample is irradiated with a radiofrequency pulse and the resulting signal is then collected. The radiofrequency pulse affects the spin state and phase coherence of the

nuclides [1, 7, 8]. A change in spin state occurs as a result of a change in energy of a spin system induced by a radiofrequency pulse; for a spin ½ nuclide this would be a transition from alignment with the applied field to alignment against the applied field, or the reverse process. Application of a radiofrequency pulse also causes the spin phases to become synchronized. Figure 1.2 illustrates the classical representation of this where the spins bunch together, a condition known as phase coherence. When the spins become coherent there is a net magnetization, coherence magnetization, precessing in the xy-plane.

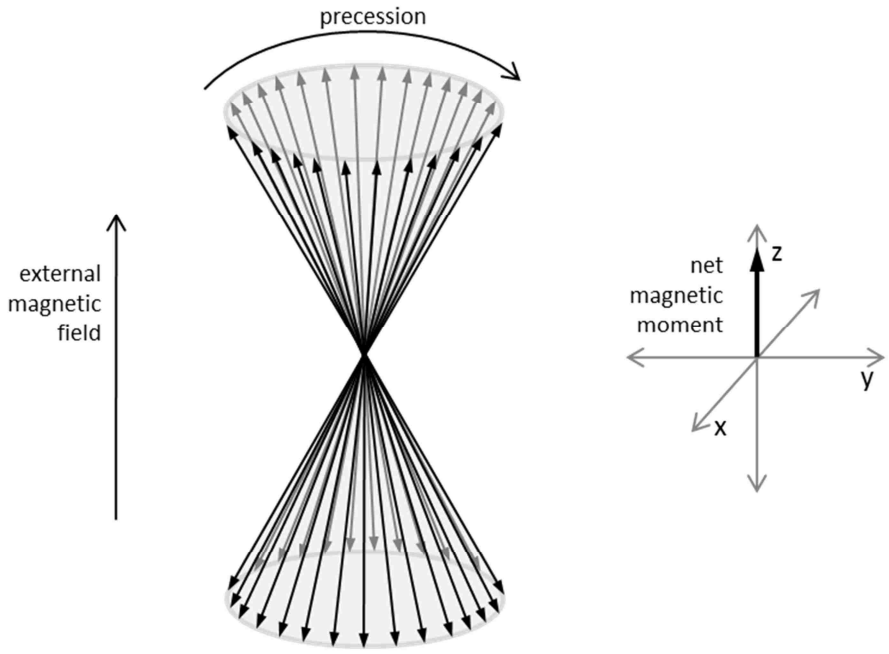

Figure 1.1. Classical representation of spin ½ nuclides in the presence of an external magnetic field and the resulting net magnetic moment

For the purpose of understanding most NMR experiments it is generally sufficient to look at the net magnetization. We will abandon focus on the individual magnetic moments involved and look at the net magnetization using the vector model in the

rotating frame of reference. In the vector model, the vectors represent the net magnetization in the coordinate axis. However, looking at the net magnetization as a vector is still complex due to precession of the magnetization about the *z*-axis. A reasonable solution is to apply the vector model to a rotating frame of reference instead of a stationary coordinate axis. In the rotating frame the coordinate axis rotates about the *z*-axis at the Larmor frequency [3]. As a result, magnetization that is precessing at the Larmor frequency appears stationary in the rotating frame.

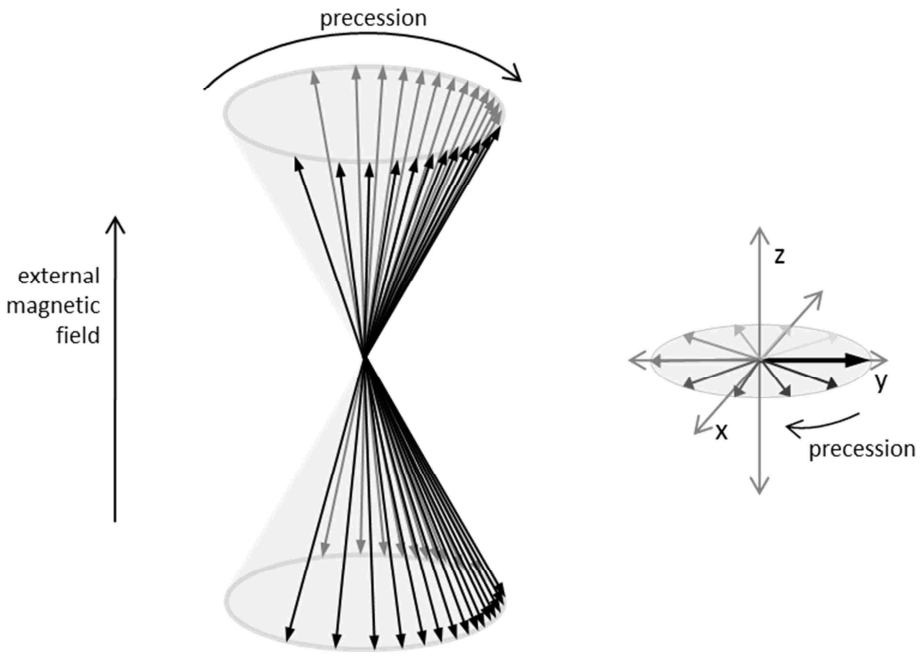

Figure 1.2. Classical representation of phase coherence caused by the application of a radiofrequency pulse on spin ½ nuclides and the resulting net magnetization

Figure 1.3 is a diagram of a standard one pulse NMR experiment and the resulting net magnetization throughout the experiment. The pulse sequence begins with a time delay, d1. This delay is necessary for the spin system to achieve thermal equilibrium before applying the 90˚ pulse. If the delay is too short the signal intensities may not be

detected at all or will be reduced and quantitative analysis will not be possible. At equilibrium the net magnetization of the sample is directed along the axis of the main magnetic field; this is designated as the *z*-axis. The sample is then irradiated with a radiofrequency pulse, referred to as a 90°_{x} pulse. This pulse rotates the magnetization by 90° about the *x*-axis; the resulting net magnetization lies along the direction of the *y*-axis. In the absence of a radiofrequency pulse the magnetization will precess about the *z*-axis of the applied magnetic field.

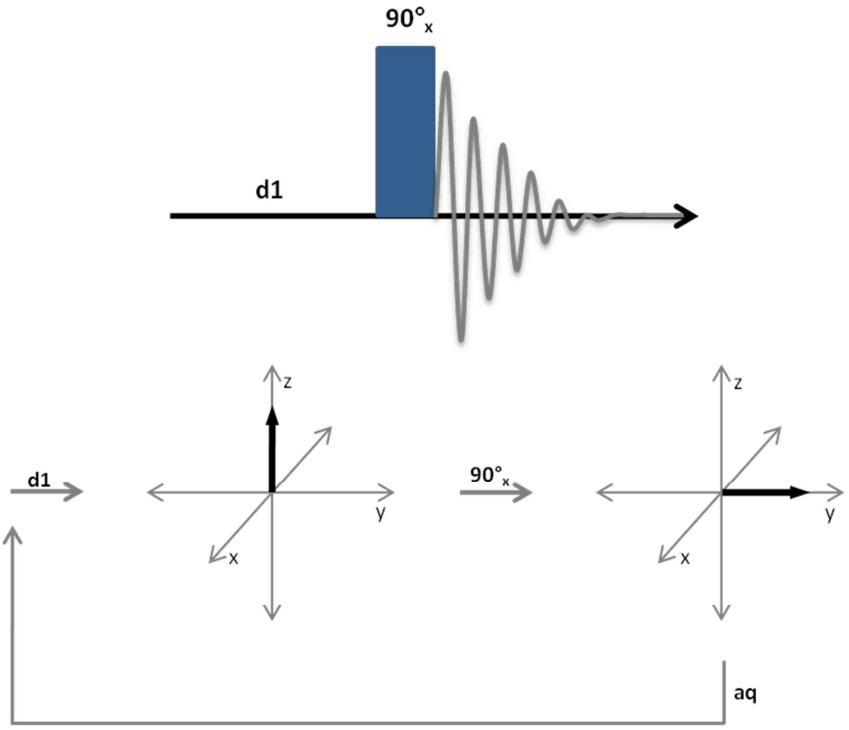

Figure 1.3. Standard one pulse NMR sequence and the resulting net magnetization throughout the experiment

Precessing magnetization in the *xy*-plane induces a current in the receiver coil [4, 5, 8]; the induced current is monitored as a function of time. The detected signal oscillates as a function of the precession of the net magnetization and decays as the

ensemble of spins return to thermal equilibrium. The resulting signal is called a free induction decay (FID). This time dependent data is then transferred to the frequency domain by Fourier transformation. The precession frequency is directly proportional to the magnitude of the magnetic field, as can be seen in Equation 4. Thus precession frequencies of 1 Hz, 2 Hz, and 3 Hz in a given magnetic field would have precession frequencies of 2 Hz, 4 Hz, and 6 Hz in a magnetic field with twice the strength. This makes comparison between data obtained at different magnetic fields problematic. Therefore, the frequency scale is generally changed to a chemical shift scale in parts per million (ppm) relative to the resonance frequency of a standard resonance [2, 3]. Equation 6 illustrates how the chemical shift, δ, is determined for a given resonance frequency, ν, where ν_{ref} is the resonance frequency of the standard. For protons the resonance frequency of protons in tetramethylsilane (TMS) is used as the reference, thus has a chemical shift of 0 ppm.

$$\delta = \frac{10^6(\nu - \nu_{ref})}{\nu_{ref}} \tag{6}$$

The process of the collection of precessing spins returning to thermal equilibrium is referred to as relaxation. Relaxation of the spins occurs by way of two processes, spin-lattice relaxation and spin-spin relaxation [1, 3, 5, 9]. Spin-lattice relaxation is a measure of the rate of interconversion between spin states to restore the equilibrium magnetization. Spin-spin relaxation is a measure of the rate of the loss of phase coherence by the spins.

1.1.1. Longitudinal Relaxation. Recovery of the longitudinal magnetization, the component parallel to the applied field, is referred to as longitudinal relaxation or spin-lattice relaxation. This process is quantified by the time constant, T_1, known as the longitudinal relaxation time constant or spin-lattice relaxation time constant.

The longitudinal relaxation time constant is generally measured using an inversion-recovery pulse sequence [1, 4, 5]. Figure 1.4 diagrams a typical inversion-recovery pulse sequence used to measure longitudinal relaxation in addition to the resulting net magnetization throughout the experiment. The pulse sequence begins with a time delay, d1, to ensure the magnetization of the sample is at thermal equilibrium before

beginning or repeating the pulse sequence. A 180°_{x} pulse is then applied which rotates the net magnetization 180˚ about the *x*-axis, thus inverting the magnetization resulting in a net magnetization directed along the negative *z*-axis. During the relaxation delay, τ, the spins begin to relax back to their equilibrium state. A 90°_{x} pulse is applied to place the partially recovered magnetization into the *xy*-plane to allow for measurement of the signal.

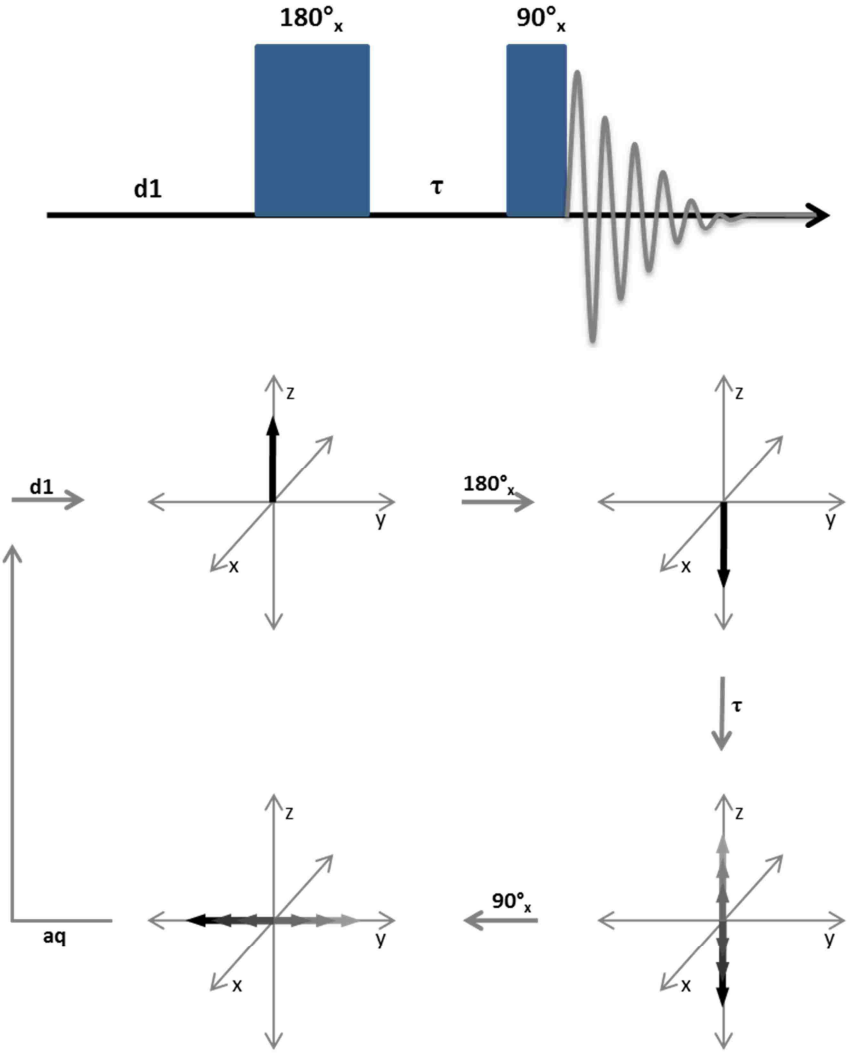

Figure 1.4. Inversion-recovery pulse sequence and the resulting net magnetization throughout the experiment

Using the inversion-recovery pulse sequence, longitudinal relaxation can be monitored by performing a series of measurements at different relaxation delay times. After short relaxation delays the net magnetization is negative; as the time allowed for relaxation increases the net magnetization becomes less negative until it disappears completely. Further increasing the relaxation delay reveals continued relaxation of the spins; the net magnetization becomes positive and increases as the relaxation delay is increased. This is shown in Figure 1.4 after the relaxation delay, where the black to light gray components indicate a range of short to long relaxation delays.

Figure 1.5 displays typical results obtained from an inversion-recovery experiment; this includes a series of data collected at various relaxation delays in addition to a plot of the signal intensity versus the relaxation delay. The signal intensity begins as a negative intensity due to the initial inversion of the magnetization. As the delay time is increased the negative signal intensity is reduced and a positive signal emerges.

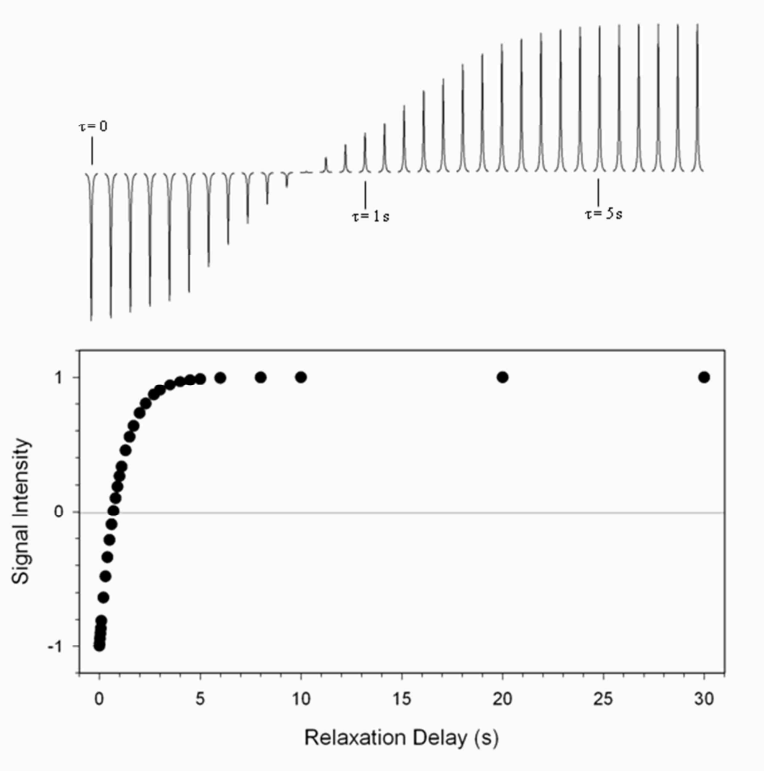

Figure 1.5. Typical results from an inversion-recovery experiment

The relaxation of the longitudinal component of magnetization is exponential in nature. The relationship between the relaxation delay, τ, and the signal intensity, M, is described by Equation 7 [1, 5, 9]. Here M_0 is the signal intensity at a relaxation delay of zero. Based on this relationship, the longitudinal relaxation time constant, T_1, can be determined by plotting the signal intensity at various relaxation delays as shown in Figure 1.5.

$$M = M_0\left(1 - 2e^{-\tau/T_1}\right) \tag{7}$$

Another common method of measuring the longitudinal relaxation time is by using a saturation-recovery pulse sequence. Figure 1.6 diagrams a typical saturation-recovery pulse sequence as well as the resulting net magnetization throughout the experiment. After the initial delay, d1, there is a long series of radiofrequency pulses, called a pulse train, with short delays in between each pulse. These pulses are generally 90˚ or less, and the delays can all be the same or varied to optimize the saturation. After the pulse train, the sample has no net magnetization and the spin system is said to be saturated. During the relaxation delay, τ, the spins begin to relax back to their equilibrium state. In contrast to the inversion-recovery pulse sequence, the magnetization is never negative in a saturation-recovery experiment. When there is no relaxation delay, there is no signal because the spins are saturated and given no time to relax. As the relaxation delay is increased the signal intensity increases, displaying recovery of the magnetization towards equilibrium. This is illustrated in Figure 1.6 after the relaxation delay; the black to light gray components correspond to a range of short to long relaxation delays. A 90°_x pulse is then applied to place the recovered magnetization into the *xy*-plane to allow for measurement of the signal.

The relationship between the relaxation delay and the signal intensity for a saturation-recovery experiment is described by Equation 8 [1, 5, 9]. Using this relationship, the longitudinal relaxation time constant can be obtained from a plot of the signal intensity versus the corresponding relaxation time.

$$M = M_0\left(1 - e^{-\tau/T_1}\right) \tag{8}$$

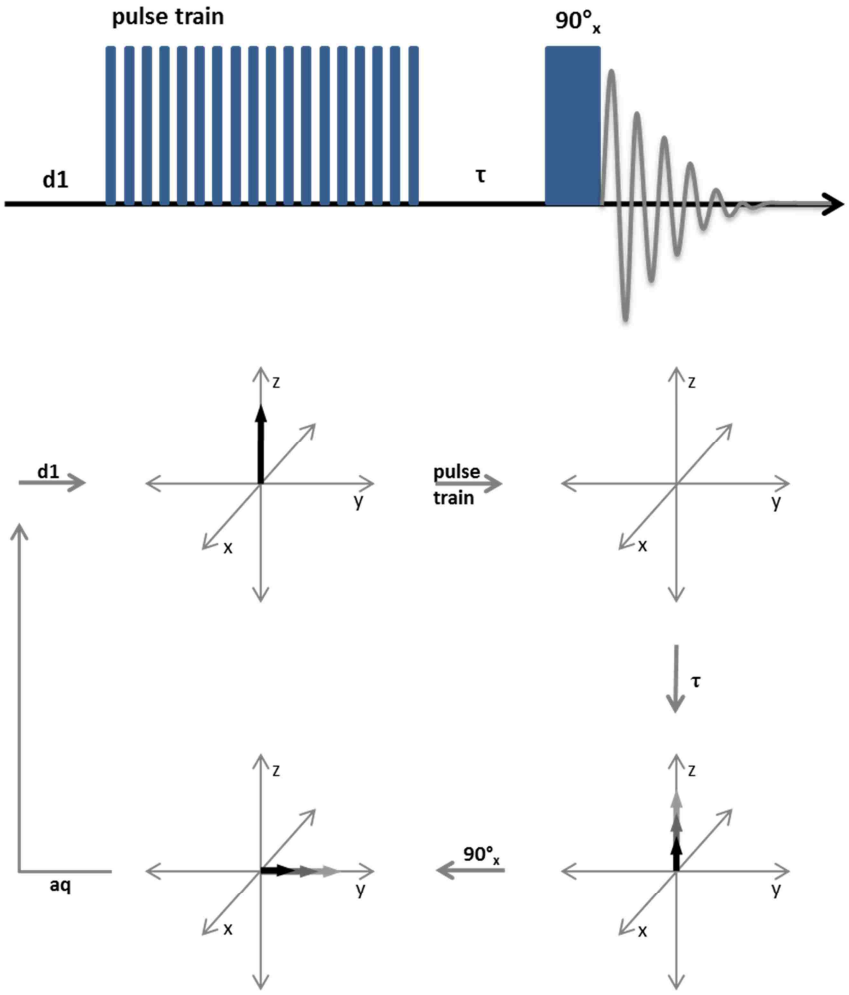

Figure 1.6. Saturation-recovery pulse sequence and the resulting net magnetization throughout the experiment

Similar to the inversion-recovery pulse sequence, obtaining a series of measurements at different relaxation delay times with the saturation-recovery pulse sequence allows observation of longitudinal relaxation. Figure 1.7 shows typical results obtained from a saturation-recovery experiment. The signal intensity begins at zero due to the initial saturation and increases as the relaxation delay time is increased.

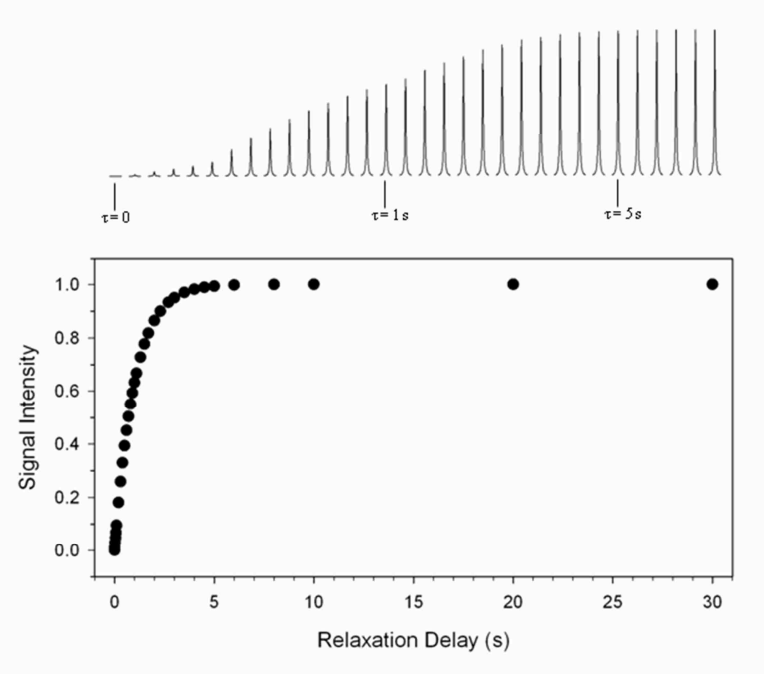

Figure 1.7. Typical results from a saturation-recovery experiment

1.1.2. Transverse Relaxation. Decay of the transverse component of the net magnetization, the component perpendicular to the direction of the applied field, is referred to as transverse relaxation or spin-spin relaxation. This process is quantified by the time constant, T_2, known as the transverse relaxation time constant or spin-spin relaxation time constant.

Transverse relaxation is generally studied using a spin-echo pulse sequence [1, 4, 10]. Figure 1.8 diagrams a typical spin-echo pulse sequence as well as the resulting magnetization throughout the experiment. The pulse sequence begins with a time delay, d1, which is sufficient for the spins to reach thermal equilibrium before beginning or repeating the pulse sequence. A 90°_x pulse is then applied, which rotates the net magnetization about the *x*-axis into the transverse plane, the *xy*-plane. During the relaxation delay, τ, the spins begin to relax back to their equilibrium state. Both transverse relaxation and longitudinal relaxation occur during this delay. In addition to relaxation, the net magnetization spreads out within the *xy*-plane due to different Larmor frequencies and inhomogenieties in the applied magnetic field. A 180°_y pulse is then

applied followed by a second relaxation delay equal to that of the first. The 180°_{y} pulse inverts the net magnetization about the *y*-axis within the transverse plane. The second relaxation delay allows time for the signals to refocus and reduces effects due to inhomogeneities in the magnetic field [4, 10].

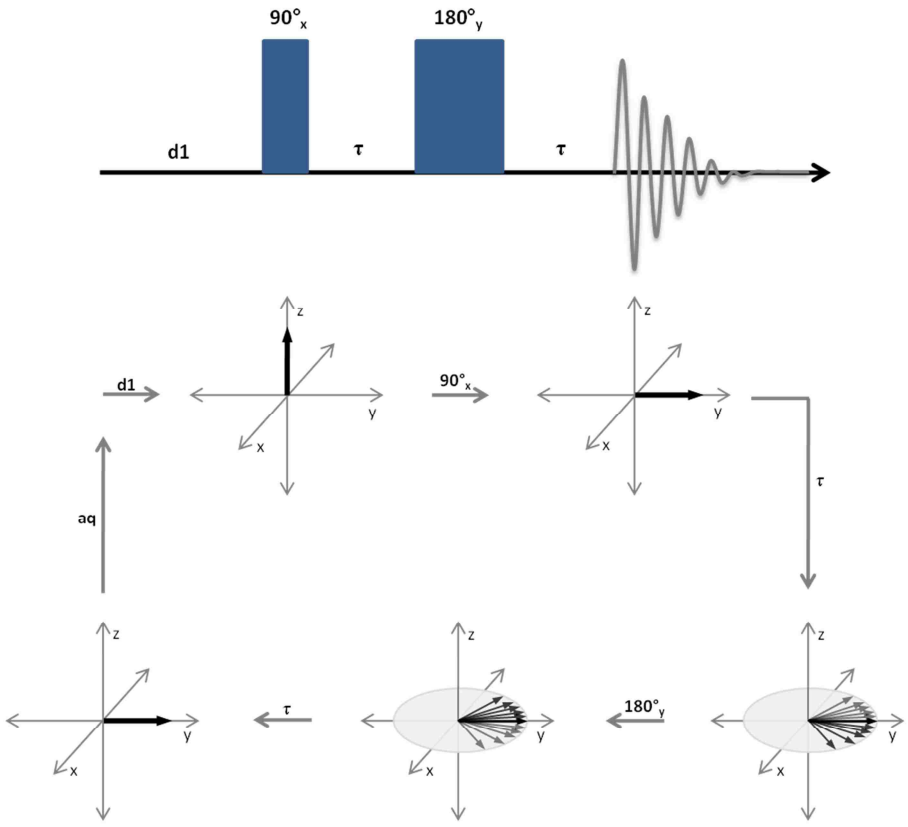

Figure 1.8. Spin-echo pulse sequence and the resulting net magnetization throughout the experiment

Transverse relaxation can be observed by monitoring the signal intensity of the magnetization after allowing it to relax for different intervals of time. As the time allowed for relaxation increases the signal intensity decreases. The relationship between

the relaxation delay, τ, and the signal intensity, M, can be described by Equation 9 [1, 5, 9].

$$M = M_0 e^{-2\tau/T_2} \tag{9}$$

Using this relationship, the transverse relaxation time constant, T_2, can be determined by plotting the signal intensity at various relaxation delays. The pulse sequence diagramed in Figure 1.8 results in a total relaxation delay of 2τ, therefore the relationship given by Equation 9 is analyzed with 2τ instead of τ. Typical results obtained by a spin-echo experiment are shown in Figure 1.9.

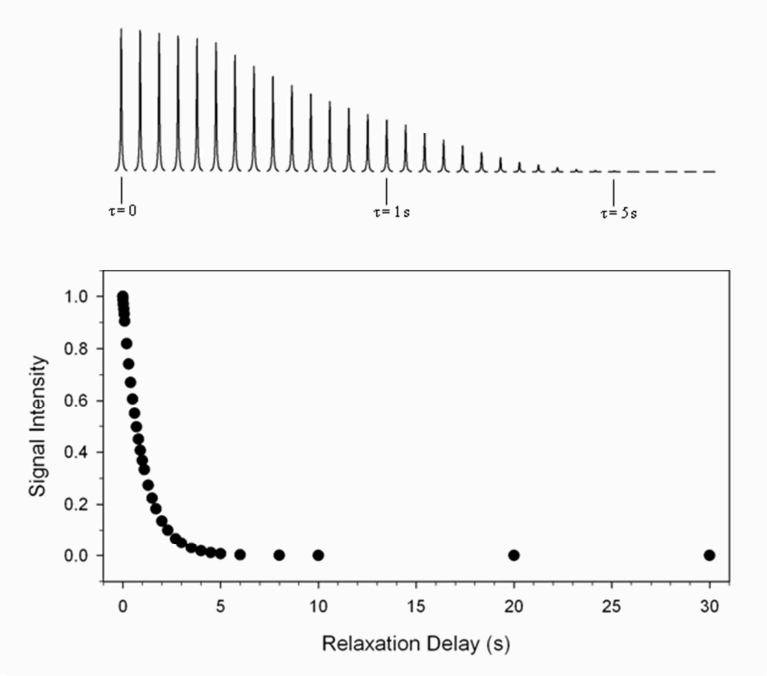

Figure 1.9. Typical results from a spin-echo experiment

1.2. SILICA AEROGELS

Silica aerogels are highly porous materials made by the sol-gel method [11]. As indicated by the name, the sol-gel method consists of preparing a sol and then a gel. A sol is a colloidal system of dispersed particles in a liquid medium. In the case of silica aerogels, the dispersed particles are silicon alkoxides and the liquid is generally an organic solvent such as methanol. A gel is also a colloidal system, but one with a solid character where the dispersed particles connect together and form a framework.

A gel is usually classified according to the dispersion medium, e.g., a hydrogel or aquagel in water, an alcogel in alcohol, an aerogel in air. When liquid is removed from a gel by evaporation, the resulting surface tension and capillary pressure due to the liquid-vapor interface can cause considerable shrinkage, cracking, and partial collapse of the gel. When there is a significant change in the gel structure due to shrinking and collapse the gel is called a xerogel instead of an aerogel. An aerogel is obtained when the liquid medium is removed with very little change to the gel structure; this usually requires special conditions to prevent significant shrinking and cracking of the gel.

Aerogels have many useful properties which are due to their porous structure. Two of the main features of the porous structure that are often focused on are the porosity and pore size. Porosity is the ratio of the pore volume to the bulk volume of the aerogel; silica aerogels normally have a porosity greater than 90%. The high porosity of aerogels leads to many unusual properties that are more characteristic of a dense gas than a solid [12]. The term pore size is somewhat deceiving considering that the pores of an aerogel don’t have a set geometric shape. Nevertheless, pores less than 2 nm are classified as micropores, ranging from 2 to 50 nm are mesopores, and greater than 50 nm are macropores [11]. Pore sizes of silica aerogels generally fall in the range of nanometers to micrometers, but the majority fall in the mesopore range. Due to the high porosity and small pore size, aerogels have very low densities and very large surface areas. Depending on preparation conditions, silica aerogels can be translucent or transparent and hydrophilic or hydrophobic. In addition, aerogels have low thermal conductivities, low refractive indices, low acoustic impedance, and low dielectric constants.

Aerogels have been considered for many applications including catalyst supports, acoustic barriers, thermal insulation, filters, thickening agents for liquid transportation,

pesticides, sensors, capacitors, desiccants, and waste containment [13]. Aerogels were first prepared in the 1930s, but there was not a significant amount of research or development of aerogels until the 1960s. The return of interest in aerogels came in parallel to the rapid development of aerogels at that time [14]; specifically the significant shortening of the preparation time which previously took more than a week. Despite the high potential of aerogels, they were not put into practical use until 1974 when they were used in Cerenkov radiation detectors. Aerogels have been the standard media for collecting cosmic dust and have been used as thermal insulation on Mars rovers [15]. In addition, aerogels have been used as thermal insulation in dual-pane windows (Super Windows) [12]. They have been used as biocatalysts by encapsulating enzymes and biosensors by immobilizing the sensor portion of the detector [16].

1.2.1. Native Silica Aerogels. Native silica aerogels are prepared by the sol-gel process, which consists of a series of hydrolysis and condensation reactions. The sol-gel process is initiated by mixing the selected precursor, water, an organic solvent, and a catalyst. Sol-gel precursors are generally tetrafunctional or trifunctional silicon alkoxides; an alternative cheaper silica source that is common for commercial synthesis is sodium silicate. Water is necessary for the hydrolysis of the precursor, but since silicon alkoxides have a low solubility in water an organic solvent is used as the dispersion medium. An acid or base catalyst can be used for the preparation of gels; three procedures are used, including acid catalysis, base catalysis, and two-step catalysis [17]. The two-step process begins in acidic solution and then a base is added to increase the rate of condensation and reduce the gelation time. Under acidic conditions hydrolysis is favored and condensation is the rate-determining step, whereas under basic conditions hydrolysis is the rate-determining step [14].

After gelation the gel is usually aged in the solution. The gel is initially very flexible. While still in solution, the neighboring hydroxyl or alkoxy groups can undergo condensation. This process is referred to as aging, which strengthens the gel and reduces the amount of shrinkage during drying. In addition, due to the reversible nature of hydrolysis and condensation, mass is dissolved from thermodynamically unfavorable regions and condenses in thermodynamically more favorable regions [14]. The dissolution and reprecipitation results in a reduction of the net curvature, disappearance

of small particles, and filling of small pores. The gel is then dried in a way to prevent collapse of the gel structure; in most cases supercritical drying is used. The solvent is put into the supercritical state and exchanged with a gas. This process eliminates the liquid-gas interface, thus there are not surface tension or capillary forces acting on the gel network during drying. The resulting aerogels are obtained with little to no shrinkage or cracking.

There are several parameters that can affect the sol-gel process, thus altering characteristics of the resulting gels. These include the choice of precursor, concentration of the precursor, water to precursor ratio, solvent used, temperature, and catalyst. The concentration of the precursor will directly affect the density of the resulting gel, while the amount of water will affect the rate of hydrolysis. The type of catalyst used influences the morphology of the gel. In general, acid catalyzed gels consist of weakly branched entangled linear chains creating a microporous structure, while base catalyzed and two-step gels consist of a network of uniform particles with more branching and larger pores [17]. Acid catalyzed gels are not only extremely weak, but the preparation time is generally significantly longer due to the slower rate of condensation. Therefore base catalysis and two-step catalysis are more commonly used than acid catalysis. Base catalyzed and two-step aerogels are formed from bead-like clusters of primary silica particles. These clusters are referred to as secondary particles. The secondary particles form a pearl-necklace type network connected by necks [18]. The pores in base-catalyzed silica aerogels are generally mesopores about 50 nm in diameter [19]. Templating and swelling agents may be used to control the pore sizes. If a sufficient amount of swelling agent is used the mesoporous structure will be destroyed, leaving a macroporous structure [20].

Aerogels have a wide variety of desirable properties, but their practical use has been limited due to some disadvantages. Aerogels are typically very fragile, brittle, hydrophilic materials. They are prone to cracking and breaking, which makes them difficult to process and limits practical use. The hydrophilicity reduces their stability in a humid atmosphere; adsorption of water will lead to cracking or even collapse of the gel structure. In addition, the expensive, risky supercritical drying step limits the use of aerogels in large scale commercial applications. All of these disadvantages have been

addressed by varying types of surface modification of the gels [19, 21]. Modifications range from simply replacing the surface hydroxyl groups with alkyl groups to crosslinking the aerogels by tethering polymers to the surface.

1.2.2. Polymer Crosslinked Silica Aerogels. The extreme fragility of native aerogels has been linked to the necks between the secondary particles. It has been shown that the silica network can be reinforced by using polymers as an interparticle crosslinker. This has been done by using the surface hydroxyl groups to begin the crosslinking. The surface hydroxyls have been used to tether diisocyanates to the surface of the silica gel [19]. These tethers then react with water forming an amine that then reacts with more diisocyanate. The resulting crosslinking is thus mostly polyurea-based with a carbamate (urethane) linkage at the silica surface [22]. A variety of polymers can be used to crosslink silica aerogels by modifying the surface of the silica gel with the appropriate functionality. For instance, the hydroxyl functionality can be replaced by an amine functionality. Similar to the hydroxyl functionality, the amine functionality can be used to crosslink with diisocyantates; this creates crosslinking that is purely polyurea-based. The amine functionality has also been used to crosslink the silica surface with polyfunctional epoxies [23] and polyfunctional styrene [24]. Silica gels have also been successfully crosslinked with methylmethacrylate, styrene, and divinylbenzene after modifying the silica surface with a free radical initiator [25].

The density, porosity, and underlying morphology of the native aerogels modified with amine functionalization and a free radical initiator stay relatively the same. When silica gels are crosslinked with polymers the material is introduced conformally to the silica network, this erases all fine particle definition. Crosslinking blocks channels to the micropores within the secondary particles, but the mesoporous network remains [19]. Retention of the mesoporous network and the high porosity also retains many of the attractive properties of native silica aerogels. In addition, crosslinking greatly improves the mechanical strength and makes it possible to machine the aerogels. Properties of the crosslinked gels depend on their density, which can be controlled by varying the concentration of the crosslinker. Increasing the density by a factor of three leads to an increase of strength by a factor of approximately three hundred [18]. The increased strength is attributed to the wider necks and flexible organic nature. The increased

strength of crosslinked gels allows the gels to withstand the surface tension forces during ambient pressure drying with hydrocarbon solvents [26]. The increase in strength is relatively the same from one polymer to another, thus it is expected that further strengthening may only be possible by modifying the underlying silica network not changing the polymer used in crosslinking [24]. However, it has been shown that the aerogels that are first modified with free radical initiator on the surface are decisively stronger than the other crosslinked aerogels [25]. This increase in strength was attributed to the longer interparticle polymer chains that resulted. The longer chains are expected to hold the structure together when even the interparticle necks are broken. In general crosslinked aerogels are found to be about ten times less hydrophilic than native aerogels [18], but styrene crosslinked aerogels are hydrophobic.

Crosslinking of silica aerogels resolves many of the drawbacks that have limited their practical use. The strengthening of the aerogel network makes both preparation and use of aerogels more feasible. The increased strength and ablility to make them hydrophobic increase their environmental stability. In addition, the increased strength allows ambient pressure drying of the gels, which can not only eliminate the risky and expensive supercritical drying step but also allows the preparation of larger aerogel samples.

2. RESEARCH OBJECTIVES

Since many of the attractive properties of aerogels are due to their porosity, pore size, and structure, it is important to be able to investigate these properties. Characteristics of porous materials – such as dimensions, size distribution, shape, and connectivity – influence fluid transport within the materials. As a result fluid transport within porous materials is often studied to give insight into these characteristics.

2.1. CONVENTIONAL METHODS

2.1.1. Porosity. Porosity, Φ, is often calculated by using the bulk density, ρ_b, and skeletal density, ρ_s, as shown in Equation 10. The bulk density can be measured by simply weighing the sample and calculating the volume based on the measured dimensions. Skeletal density requires the measurement of the volume of the solid network; this can be done by submerging the sample into a liquid and measuring the displacement, but this would then require drying the aerogel sample again. Alternatively, helium pyknometry can be used to measure skeletal density.

$$\Phi = \frac{{}^{1}/_{\rho_b} - {}^{1}/_{\rho_s}}{{}^{1}/_{\rho_b}} \times 100\% \tag{10}$$

2.1.2. Pore size. The pore size and structure are analyzed by a variety of methods. Nitrogen adsorption/desorption according to the Brunauer, Emmet, and Teller (BET) method is probably the most widely used method to measure the surface area and pore size distributions in aerogels. Nitrogen adsorption/desorption is said to detect pores that are accessible to nitrogen [14]. However, while nitrogen can access pores down to about 0.7 nm, it is estimated to only see pores smaller than 50 nm in diameter [27]. Therefore nitrogen adsorption/desorption should only be used for information regarding mesoporous materials; it is not expected to be reliable for macroporous materials and can only access portions of microporous materials. Mercury porosimetry is also a common method of measuring pore size and volume in porous materials, but the pressures required for penetration of mercury are likely to damage the aerogel network. Mercury can

penetrate pores as small as 7 nm with application of a significant amount of pressure, but it is generally considered only a representative method for macroporous materials [27]. Adsorption/desorption and porosimetry methods require an assumption of pore shape to relate the results with characteristics such as the pore radius, and they often are only a measure of the smallest constriction in a pore rather than the average radius [28]. Also, the pressures required for adsorption/desorption and porosimetry can lead to dilation and constriction of the pores resulting in false results. Electron microscopy techniques are often used to study the morphology and can be used to estimate the pore size; however, the high energy of the electron beam can cause alteration of the sample. In addition, to gain an adequate representation of the sample a large amount of images must be processed. Adsorption/ desorption, porosimetry, and electron microscopy all require a dried sample and are destructive to the sample.

Porous materials may also be analyzed using small-angle scattering techniques. The combination of small-angle light scattering (SALS) with ultrasmall- and small-angle X-ray scattering (USAXS and SAXS) methods cover the entire spatial scale of aerogels (< 1 nm to > 5 μm) [29]. While this combination of techniques is not destructive and not sensitive to pore connectivity or network effects, none of the methods are widely used for characterization of porous materials.

No technique can provide complete information about the pore structure, a combination of methods must be used to gain a true view of the porous structure. Although technique limitations should be carefully considered, the shortcomings of these methods are often overlooked in general use. For silica aerogels, nitrogen adsorption/desorption using the BET method is the most common technique of measuring the porous surface area. Silica aerogels tend to be predominately mesoporous, but the microporous and macroporous surfaces are not accurately measured using BET.

2.2. NMR METHODS

NMR is a nondestructive technique that can be used to investigate both static and dynamic systems [4, 5, 6]. Porous materials may contain micropores, mesopores, and macropores; generally the NMR technique utilized to characterize each of these is

different [30]. Differences in chemical shift, relaxation, and diffusion can all be used to selectively probe systems monitored by NMR.

2.2.1. Porosity. Quantitative NMR analysis of a filling fluid in porous media can be used to determine the porosity[31]. The signal intensity is proportional to the number of nuclear spins. The ratio of the signal intensity of the fluid within the pores, I_{pore}, to the signal intensity of the bulk liquid, I_{bulk}, gives a measure of the porosity, as shown in Equation 11.

$$\Phi = \frac{I_{pore}}{I_{bulk}} \times 100\% \tag{11}$$

2.2.2. Pore size. NMR chemical shift arises from different environments. The varying sizes of pores in porous media would be expected to result in signals with different chemical shifts. However, the exchange between mesopores and macropores is generally rapid, resulting in line broadening and difficulty in distinguishing the differences in environments. In addition, molecules in different parts of the pores feel different magnetic fields due to magnetic susceptibility differences between the solid and fluid and the presence of paramagnetic species. The inhomogeneities in the magnetic field lead to broadening of the resonance line due to varying frequencies. The broad lines indicate differing environments but cannot easily be correlated to pore characteristics. Even when the magnetic susceptibility and paramagnetic affects are negligible, relaxation effects can cause line broadening. Thus chemical shift analysis of NMR spectra is not sufficient to characterize mesoporous and macroporous materials.

In microporous materials the fluid is essentially always in contact with the surface, resulting in spectra that are dominated by surface effects. When surface effects dominate the spectra, chemical shift can be used as a probe for microporous materials. Information about the pore size of microporous materials is generally obtained from the chemical shift of ^{129}Xe NMR. In comparison to other filling fluids used to probe porous materials, xenon is highly polarizable resulting in a high sensitivity to its environment. The high polarizability leads to a large chemical shift range, between 0 and 250 ppm, which results in sufficient resolution to distinguish micropores. The chemical shift can be related to the dimensions of the pores, wall curvature, and surface-to-volume ratio [32].

NMR relaxation times are sensitive to molecular motion, thus they can be used to probe the dynamics of molecules [4, 5]. A longer relaxation time indicates greater mobility whereas a shorter relaxation time indicates restricted mobility. The relationship between mobility and relaxation time can be used to study porous media by measuring the relaxation time of a filling fluid. Fluid at the surface of the pores will have a reduced mobility, resulting in a reduced relaxation time. The reduced relaxation time results from attraction between the fluid and the surface, which is a short range dipole-dipole interaction. In addition, paramagnetic sites on the surface can also contribute to the enhanced relaxation time.

A two-site model is often employed to analyze the relaxation data from fluids within porous media [30, 31, 33-35]. This model is based on the proposal that the fluid molecules occupy one of two sites; the fluid molecules are either at the surface of the pores or within the pore. The fluid molecules at each site have a different relaxation time; the molecules at the pore surface will have an enhanced relaxation time and the molecules within the pore will have a relaxation time similar to bulk liquid. The observed relaxation time, T, is related to the relaxation time of the molecules at the pore surface, T_S, and the molecules within the pores, T_B, as shown in Equation 12. The rate of relaxation observed is a weighted average of the relaxation rates of the molecules at each of these sites, where x is the fraction of molecules at the pore surface.

$$\frac{1}{T} = \frac{x}{T_S} + \frac{(1-x)}{T_B} \tag{12}$$

The fraction of molecules at the surface is directly related to the surface-to-volume ratio, S/V, and the thickness of the surface layer, Δ. Substituting this relationship into Equation 12 reveals a correlation between the observed relaxation time and the pore structure as shown in Equation 13. A further simplification to Equation 13 is made by considering the thickness of the surface layer and the difference in the relaxation rates of the two sites as a function of the surface. The product of the surface layer thickness and the difference in the relaxation rates between the surface and the bulk are combined into one parameter called the surface relaxivity parameter, ρ, as shown in Equation 14. The

surface relaxivity parameter has units of velocity and is a measure of the rate at which the nonequilibrium magnetization leaves the molecules near the surface.

$$\frac{1}{T} = \frac{1}{T_B} + \frac{S\Delta}{V}\left(\frac{1}{T_S} - \frac{1}{T_B}\right) \tag{13}$$

$$\frac{1}{T} = \frac{1}{T_B} + \frac{S}{V}\rho \tag{14}$$

In some instances the relaxation time of the bulk liquid is much greater than the liquid in the porous media. If the bulk relaxation time is much larger than the relaxation time at the surface sites then the relaxation rate of the bulk fluid is not significant and the observed relaxation rate can be directly related to the surface to volume ratio as shown in Equation 15. However, the simplification of removing the bulk relaxation rate from Equation 14 is generally only true for materials with pore sizes smaller than 5 nm [33] or materials with a high paramagnetic content.

$$\frac{1}{T} \approx \frac{S}{V}\rho \tag{15}$$

The surface-to-volume ratio can be correlated to a pore dimension if the pore shape is assumed, for instance, the pore radius if a spherical pore shape is assumed. Generally the interest in the pore size is related to the transport properties instead of the specific shapes of the pores, so the volume-to-surface ratio is sometimes considered to be a measure of the hydraulic radius [33]. Substituting this into Equation 14 gives an expression relating the observed relaxation rate to the hydraulic radius, r_h, as shown in Equation 16.

$$\frac{1}{T} = \frac{1}{T_B} + \frac{\rho}{r_h} \tag{16}$$

Further modifications have been made to the two-site model incorporating differences due to the wettability of the liquid and the size of the pores. The wettability of a liquid is the measure of affinity of the porous material to one liquid over another. The

expression given in Equation 16 is generally considered to be applicable for wetting liquids down to a pore radius of 1.8 nm [30]. However, for nonwetting liquids significant deviations are observed with pore radii of less than 3 nm. Equation 17 incorporates an additional term to account for the deviation, where *c* is a constant, *a* is the relaxation rate of the bulk fluid ($1/T_B$), and *b* is the surface relaxivity. In this relationship *a* is purely a function of the fluid, temperature, and magnetic field, whereas *b* is has additional contributions from the surface chemistry and *c* is related to geometrical factors.

$$\frac{1}{T} = a + \frac{b}{r_h} + \frac{c}{{r_h}^2} \tag{17}$$

If diffusion within a pore is not rapid, then more than one relaxation time would be observed for the pore and values would depend on the detailed pore geometry and not just the surface-to-volume ratio. If the rate of pore coupling is fast, the sample will experience uniform magnetization behavior and the observation of a single relaxation time related to the surface-to-volume ratio of the entire sample instead of relaxation times related to the individual pores. In general, for pore sizes less than 1 µm there will be one relaxation time observed [34].

The above equations were presented in a generic form including an observed relaxation time, *T*. Equations 12-17 are generally presented as being applicable to both spin-lattice relaxation time, T_1, and spin-spin relaxation time, T_2. However, caution should be taken when using them for spin-spin relaxation, because the T_2 relaxation time is greatly affected by diffusion of the molecules in the presence of local magnetic field gradients [30]. To obtain accurate T_2 values in the presence of local gradients, short echo spacings and a low magnetic field should be used. Otherwise, the two-site model must be modified by adding a term to account for effect of the diffusion within the local magnetic field gradients [35]. The addition of diffusion measurements yields more confidence in understanding the pore structure, but significantly increases the difficulty of analysis required. Some authors disagree to the use of T_1 as a probe of pore characteristics because the spin-lattice relaxation time does not reveal information about tortuosity or connectivity [36]. The tortuosity is used to relate the actual distance traveled by a molecule to the net distance traveled.

The two-site model is considered to be a fair representation, but one must be cautious of the limitations of the model. Knowledge of the surface relaxivity parameter is required to relate the observed relaxation time with pore characteristics. The surface relaxivity is generally assumed to be constant for a particular sample. Sometimes the surface relaxivity of different materials are considered to be similar enough so that NMR relaxation measurements can be used for estimates of surface-to-volume ratios [37]. Alternatively, an independent measurement of the surface-to-volume ratio can be used to determine the surface relaxivity, but the result will vary depending on the technique used to measure the surface-to-volume ratio due to the differing sensitivities of different length scales. Equation 18 illustrates a common method used to calculate the surface-to-volume ratio based on independent measurements of porosity, specific surface area, S_S, and bulk density, ρ_b.

$$\left(\frac{S}{V}\right)_{pore} = \frac{(1-\Phi)}{\Phi} S_S \rho_b \tag{18}$$

Some considerations must be taken when using the two-site model. The model assumes diffusion within a pore is rapid and assumes that diffusion between pores of different dimensions is slow. If diffusion within a pore is slow then a distribution of relaxation times will be observed and the mathematical analysis can become problematic. Magnetic susceptibility differences between the fluid and solid phase can also complicate the analysis of spin-spin relaxation. The nature of the surface has been shown to affect the relaxation times [28, 34] and must be taken into consideration when interpreting results. As can be seen in Equation 14, changes in the surface area and the surface relaxivity have an equal potential to affect the observed relaxation time. A reduction in the surface roughness and an increase in the paramagnetic sites on the surface have been studied using the sorption of oil [35]. The reduction of surface roughness will directly affect the surface-to-volume ratio, and the increase in paramagnetic sites will increase the surface relaxivity. Additional concerns towards using the two-site model as a general tool include the effect of pore shape and how to correct for the volume of the surface layer when studying small pores [28].

The above studies of pore filling fluid are often done at room temperature with one filling fluid. Monitoring the relaxation time at different temperatures and relaxation studies with more than one filling fluid have also been explored. The freezing point of a liquid inside of a porous solid is lower than that of bulk liquid. The frozen fluid will have a short relaxation time that can be easily eliminated and the NMR peak area from the liquid fluid can be analyzed as a function of temperature. Temperature studies in porous materials are only appropriate for mesoporous materials. When the pore size becomes too small the strong adsorption at the surface has a large effect which is difficult to model [30]. In addition, the use of two immiscible fluid phases has also been used to characterize porous materials [38]. Analysis of NMR relaxation as a function of the mixing ratio can help to focus on the surface layer and the bulk pore fluid individually if one has a strong affinity for the pore surface compared to the other. Furthermore, it may be possible to selectively probe one of the liquids based on chemical shift or relaxation differences.

3. MATERIALS AND METHODS

3.1. AEROGEL SAMPLES

Both native and polymer crosslinked silica aerogels were analyzed using NMR. Native silica aerogels were synthesized directly in 5 mm NMR tubes. The crosslinked aerogels were machined to fit snuggly into the bottom of standard 5 mm NMR tubes. The gels were then placed in tubes filled with a mixture of acetone and deuterated acetone (acetone-d_6). Thus the void space in the aerogels was filled with solvent, resulting in a saturated gel in the bottom half of the measuring area and bulk solvent in the top half of the measuring area, as illustrated in Figure 3.1.

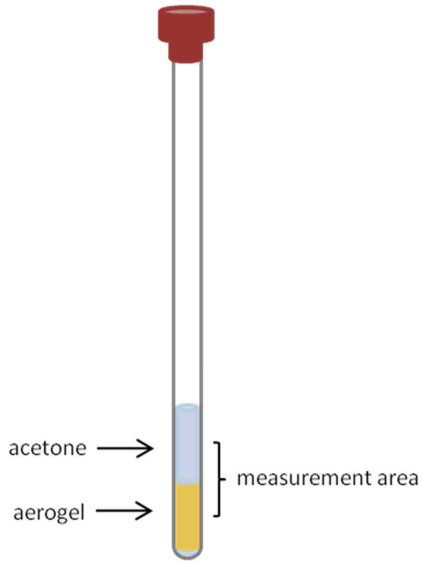

Figure 3.1. Silica aerogel submerged in acetone in 5 mm NMR tube

The samples analyzed are listed in Table 3.1, including the abbreviation and composition. The gels were synthesized by acid or base catalysis, as indicated. Base-catalyzed gels were prepared by mixing a solution of methanol and ammonium hydroxide with a solution of methanol and TMOS. Acid-catalyzed gels were prepared from a

solution of methanol, potassium hydrogen pthalate, and hydrochloric acid mixed with a solution of methanol and TMOS. The crosslinking agents include diisocyanate, methylmethacrylate, and styrene, where X indicates gels crosslinked with diisocyanate. All of the aerogels labeled with MP4 were templated using 4 g Pluronic P123 [20]. TMB was used as a swelling agent for some of the templated samples as indicated by the T in the abbreviation, with the amount of swelling agent given in Table 3.1.

Table 3.1. Aerogel samples analyzed with NMR

Abbreviation	**Composition**
BC	Native base catalyzed silica aerogel
X-BC	Base catalyzed silica aerogel crosslinked with diisocyanate
AC	Native acid catalyzed silica aerogel
X-AC	Acid catalyzed silica aerogel crosslinked with diisocyanate
MP4	Native acid catalyzed silica aerogel prepared with 4 g Pluronic P123
X-MP4	Acid catalyzed silica aerogel prepared with 4 g Pluronic P123 and crosslinked with diisocyanate
MP4-T045	Native acid catalyzed silica aerogel prepared with 4 g Pluronic P123 and 0.45 g TMB
X-MP4-T045	Acid catalyzed silica aerogel prepared with 4 g Pluronic P123, 0.45 g TMB, and crosslinked with diisocyanate
MP4-T065	Native acid catalyzed silica aerogel prepared with 4 g Pluronic P123 and 0.65 g TMB
X-MP4-T065	Acid catalyzed silica aerogel prepared with 4 g Pluronic P123, 0.65 g TMB, and crosslinked with diisocyanate
MP4-T200	Native acid catalyzed silica aerogel prepared with 4 g Pluronic P123 and 2.00 g TMB
MP4-T310	Native acid catalyzed silica aerogel prepared with 4 g Pluronic P123 and 3.10 g TMB
X-MP4-T310	Acid catalyzed silica aerogel prepared with 4 g Pluronic P123, 3.10 g TMB, and crosslinked with diisocyanate
Si-AIBN	Native base catalyzed silica aerogel with AIBN surface modification
50% MMA	Base catalyzed silica aerogel with AIBN surface modification crosslinked with 50% MMA
50% styrene	Base catalyzed silica aerogel with AIBN surface modification crosslinked with 50% styrene
75% styrene	Base catalyzed silica aerogel with AIBN surface modification crosslinked with 75% styrene

3.2. MATERIALS AND INSTRUMENTATION

The aerogel samples were machined using a Proxxon PD 230/E micro lathe. The acetone used was HPLC grade; it was purchased from Fisher Scientific and used without purification. Acetone-d_6 (99.9% deuterium) was purchased from Cambridge Isotope Laboratories. NMR tubes were obtained from Norell, all having a 5 mm diameter and a minimum grade of 300 MHz or higher. A 200 MHz, 89 mm wide-bore Bruker Avance NMR Spectrometer was used to analyze the aerogel samples.

3.3. RELAXATION MEASUREMENTS

Relaxation times for both the bulk solvent above the aerogel and for the solvent within the aerogel were measured simultaneously. The NMR measurements were done using a gradient-recalled echo technique to obtain T_1- and T_2-weighted profiles. The profiles were then analyzed to obtain independent relaxation times for the bulk solvent and the solvent within the pores.

3.3.1. Relaxation-Weighted Profiling. A gradient-recalled echo technique was used to obtain T_1- and T_2-weighted profiles. This was done using the respective relaxation pulse sequence integrated with a standard gradient-recalled echo imaging sequence. An imaging technique was chosen to allow simultaneous acquisition of the bulk fluid and the pore filling fluid. The gradient pulse used creates a linear magnetic field gradient along the direction of B_0 (the z-axis) [1, 39, 40]. As a result the spins experience different field strengths depending on their position along the z-axis. Since the precession frequency is directly proportional to the strength of the applied field, the spins exposed to a higher magnetic field will precess at a higher frequency and the spins exposed to a lower magnetic field will precess at a lower frequency. Thus, during the application of a gradient pulse the precession frequency of each spin is directly related to its position along the z-axis. After the gradient pulse is turned off, all of the spins return to precession at the Larmor frequency. However, the magnetic moments of the spins will be phase shifted as a result of the gradient pulse. Figure 3.2 diagrams the resulting magnetic moments after a gradient pulse.

Proper application of gradient pulses can result in either frequency or phase encoding of the magnetic moments with respect to their location along the z-axis [4, 39, 40]. If frequency encoding is desired the gradient pulse should be executed during the

signal acquisition. Application of a gradient pulse before signal acquisition will result in phase encoding. Both techniques can be utilized for imaging purposes; our images were obtained through a frequency encoding method.

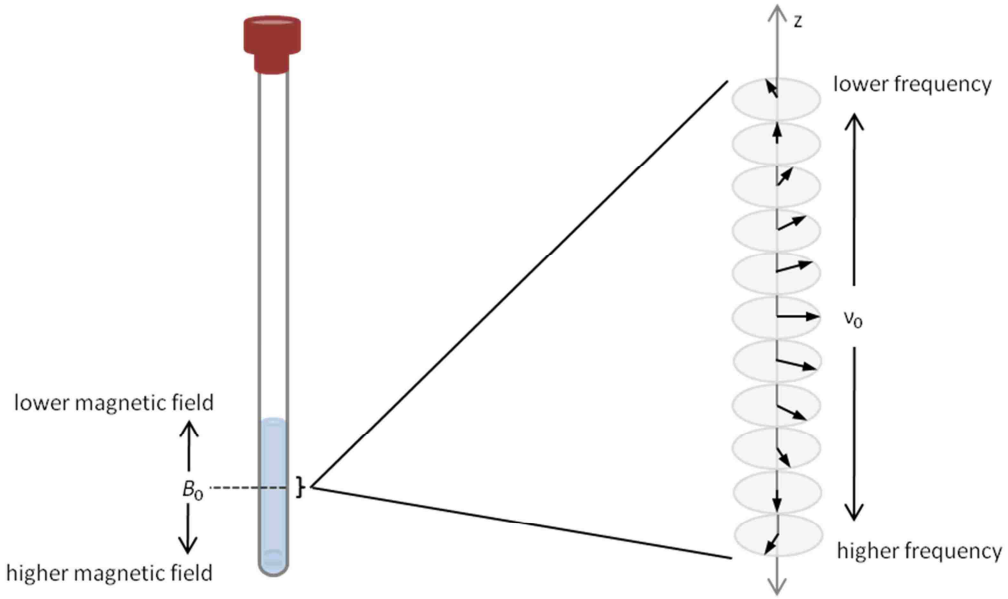

Figure 3.2. Resulting magnetic moments after a gradient pulse

3.3.2. Transverse Relaxation Profiles. T_2-weighted relaxation profiles were acquired using a combination of a Carr-Purcell-Meiboom-Gill (CPMG) spin-echo pulse sequence [5, 10] and a gradient-recalled echo imaging technique. Figure 3.3 diagrams the pulse sequence and the fate of the magnetization throughout the experiment.

The initial delay, d1, allows time for the spin system to reach thermal equilibrium. After the 90°_x pulse the net magnetization is directed along the *y*-axis. During the delay, τ, the spins begin to relax and dephase. A 180°_y pulse followed by a second delay, τ, is applied to refocus the spins. A constant gradient pulse is then applied for a time equal to the delay d2 which causes the spins to precess at a frequency dependent on their location along the *z*-axis. After the gradient pulse the spins return to precession at the Larmor

frequency but are phase shifted do to the gradient pulse. A 180˚$_y$ pulse then rotates the spins about the *y*-axis. The 180˚$_y$ pulse is surrounded by short delays of d3 to allow for electronics switching. A second gradient pulse is then applied at a delay time of d4 before the acquisition of the FID begins. Due to the 180˚$_y$ pulse the spins that were exposed to the higher magnetic field during the first gradient pulse are now exposed to a lower magnetic field, thus precess at a lower frequency. Similarly, the spins that were exposed to the lower magnetic field during the first gradient pulse are now exposed to a higher magnetic field, thus precess at a higher frequency. The change in the experienced magnetic field results in a refocusing echo of the spins during the gradient pulse. The signal is acquired during this echo.

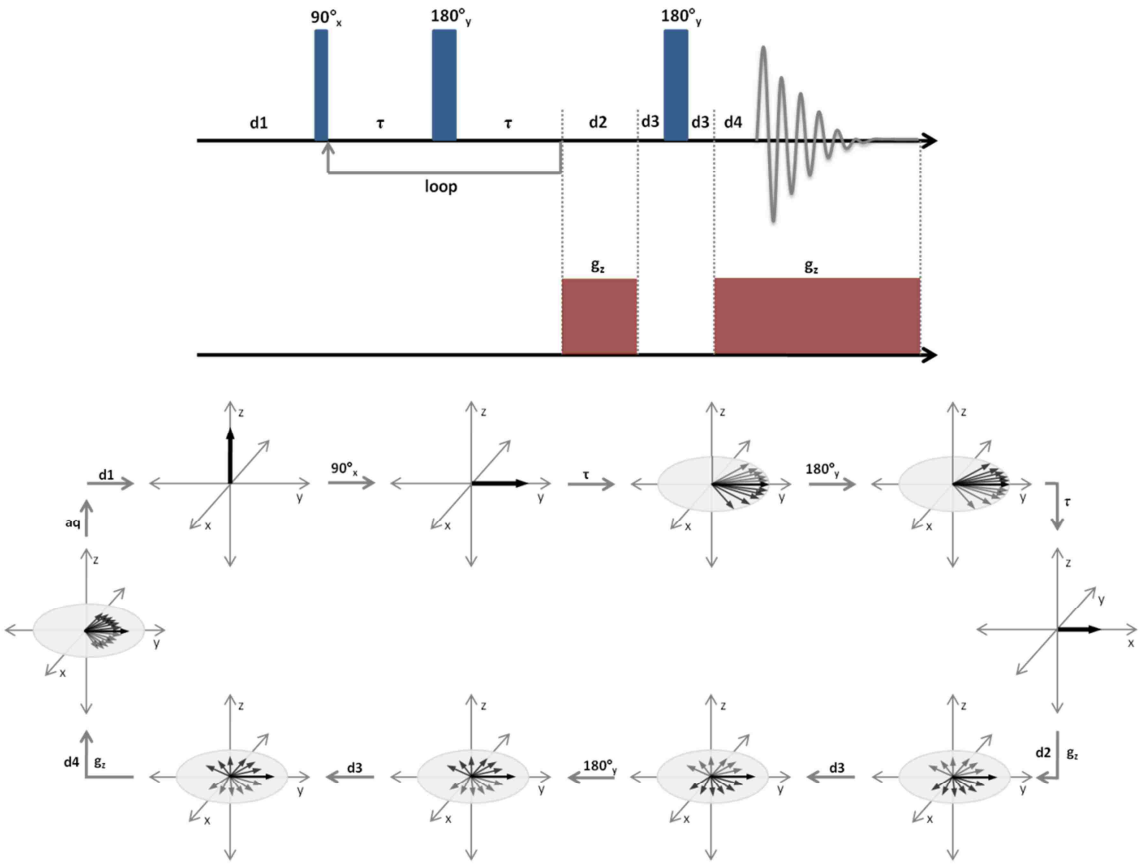

Figure 3.3. CPMG spin-echo T_2-weighted profile pulse sequence and corresponding fate of magnetization throughout the experiment

In the pulse sequence shown in Figure 3.3, the gradient pulse is applied during the signal acquisition. Applying a gradient pulse during signal acquisition leads to spin frequencies that correspond to the position along the *z*-axis. Therefore, the frequency spectrum is actually a profile along the *z*-axis.

3.3.3. Longitudinal Relaxation Profiles. T_1-weighted relaxation profiles were acquired using two methods. The first included an inversion-recovery pulse sequence and the second method used a saturation recovery pulse sequence. Similar to the T_2-weighted profiles, both pulse sequences were integrated with a gradient-recalled echo imaging technique. Figure 3.4 illustrates the pulse sequence and the resulting magnetization throughout the sequence for the inversion recovery method.

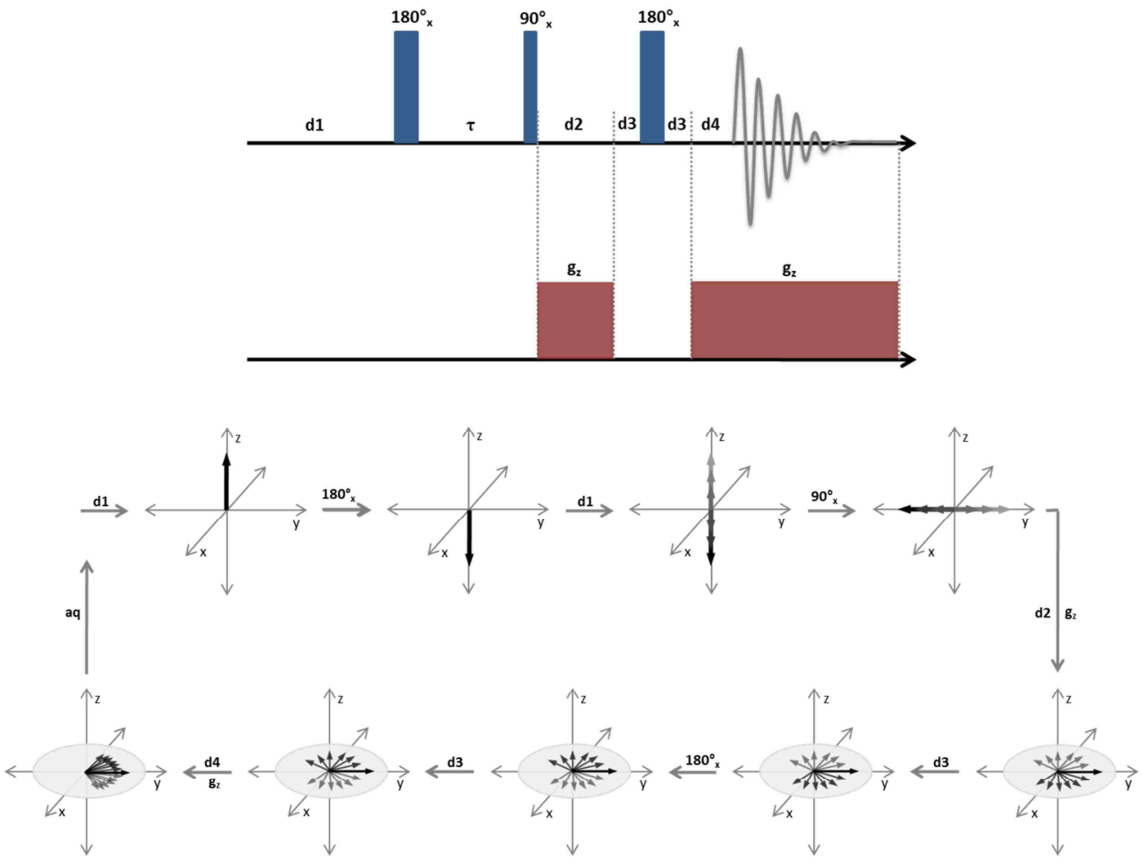

Figure 3.4. Inversion recovery T_1-weighted profile sequence with corresponding magnetization throughout the experiment

The pulse sequence begins as a standard inversion-recovery pulse sequence. First is a time delay, d1, which is sufficient time for the spin system to reach thermal equilibrium. A 180°_{x} pulse is applied to invert the magnetization, followed by a delay to allow for relaxation. A 90°_{x} pulse is applied to rotate the magnetization into the transverse plane for observation. In contrast to a standard inversion-recovery pulse sequence, the signal is not immediately observed after moving the magnetization into the transverse plane. Analogous to the procedure used for the T_2-weighted relaxation profile, gradients are used to produce a T_1-weighted relaxation profile. The combination of gradient and 180°_{y} pulses results in a spectrum in which the precession frequency depends on the location along the *z*-axis.

Using an inversion-recovery pulse sequence, the signal will start out as a negative (inverted) signal at short delay times. As the delay time is increased, the signal will become less negative. At an intermediate delay time the signal will become zero. Upon increasing the delay time further, the signal will become positive (recover) until it reaches equilibrium. To obtain the T_1-weighted profile, a magnitude calculation must be performed on the data to remove the phase encoding. The magnitude calculation results in all positive signals, which leads to difficulty in analyzing the data. Before the T_1 relaxation times can be calculated from the data, the signals must be manually converted to negative signals where appropriate.

An alternative to using the inversion-recovery pulse sequence to measure T_1 relaxation times is to use a saturation-recovery pulse sequence. Using a saturation-recovery pulse sequence solves the problem caused by the magnitude calculation, because all of the resulting signals from this pulse sequence are positive. Like the previous pulse sequences, a standard 1D imaging pulse sequence was added to the saturation-recovery pulse sequence to obtain T_1-weighted profiles. The pulse sequence is shown in Figure 3.5. An additional benefit to using the saturation-recovery pulse sequence is that only a short delay is required between each scan. Normally, there must be a long enough delay between the scans to allow the signal to fully relax before the next scan, but a saturation-recovery pulse sequence begins by saturating the signal which eliminates the need for full relaxation between the scans. An initial delay is still included because short delay is necessary to allow electronics switching.

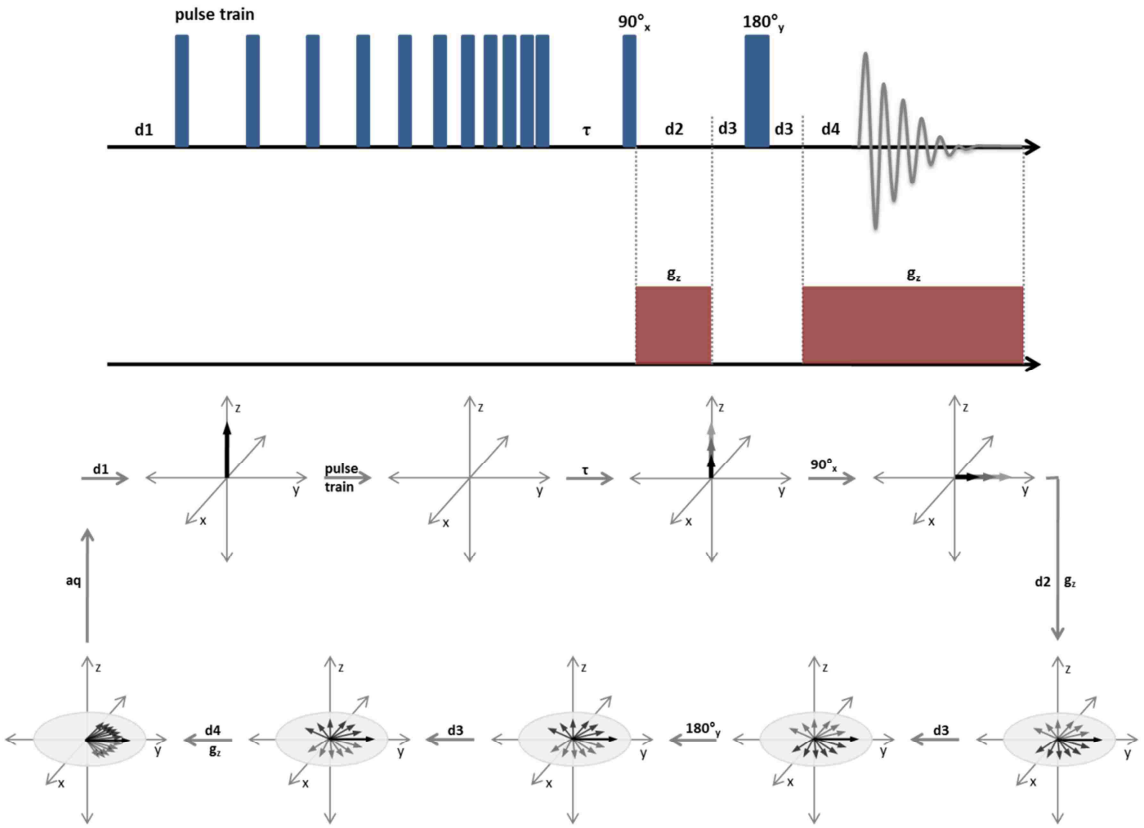

Figure 3.5. Saturation recovery T_1-weighted profile sequence with corresponding magnetization throughout the experiment

The pulse sequence begins exactly as a standard saturation-recovery pulse sequence. After the initial time delay, d1, a pulse train is applied to saturate the magnetization. After a delay, τ, to allow for relaxation, a 90°_{x} pulse is applied to rotate the magnetization into the transverse plane for observation. Then gradients are used to produce a T_1-weighted relaxation profile in which the precession frequency depends on the location along the *z*-axis.

The saturation-recovery pulse sequence shown in Figure 3.5 was modified further for some of the polymer crosslinked aerogels. The intent of the experiment was to measure the T_1 relaxation of the solvent within the aerogel and the bulk solvent above the aerogel. However, the protons in the crosslinking polymers may also be detected with the original pulse sequences. The addition of the two relaxing signals results in a total signal

with a relaxation time that is a weighted average of the relaxation times of each component. Figure 3.6 shows plots of two scenarios, in the top plot a case where the amount of signal from the polymer is comparable to the amount of signal from the pore liquid, and in the bottom plot in which the amount of signal from the polymer is very small compared to the amount of signal from the pore liquid. In cases where the amount of signal from the polymer is significant, the relaxation time calculated will be shortened due to the addition of the faster relaxing polymer signal.

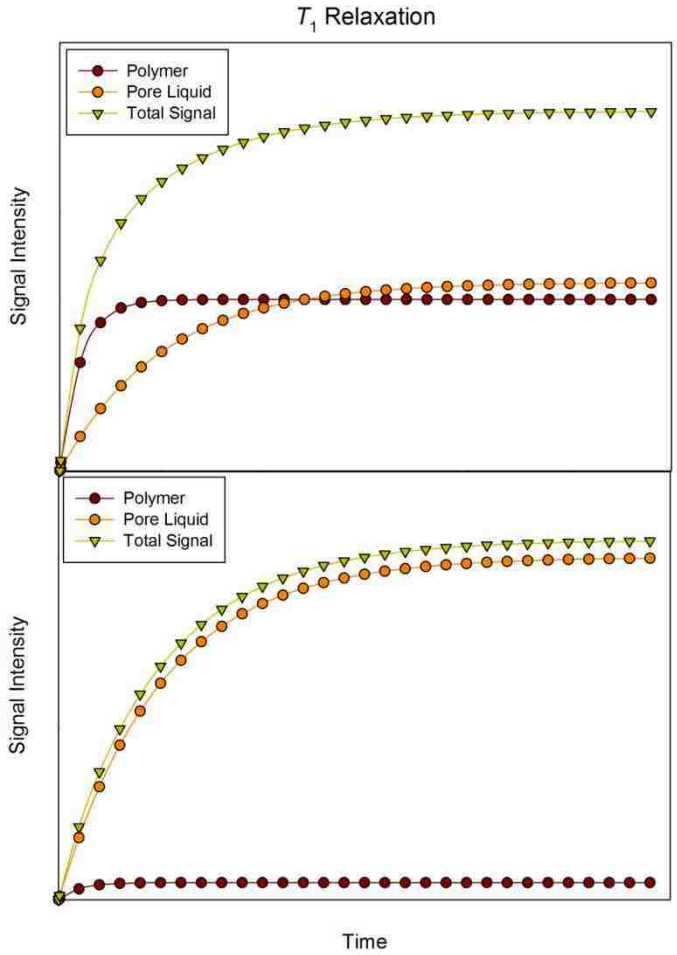

Figure 3.6. Comparison of polymer T_1 relaxation, pore liquid T_1 relaxation, and the resulting total T_1 relaxation

The T_1 relaxation times of the polymer signal and the pore liquid were too close to be able to selectively eliminate the polymer signal using T_1 relaxation. However, the T_2 relaxation times of the polymer signal and the pore liquid, about 1 ms and 25 ms respectively, are sufficiently different to allow for selective elimination of the polymer signal by T_2 relaxation. Figure 3.7 shows a plot comparing the T_2 relaxation of the polymer signal and the pore liquid. Inserting a delay after the magnetization is returned to the transverse plane allows for the polymer signal to be selectively removed. The gray area in Figure 3.7 represents the delay necessary to remove the polymer signal. The T_2 relaxation delay is added between the 90°_x pulse and the gradient pulse in the sequence shown in Figure 3.5. The additional delay allows the polymer signal to fully relax before acquiring the signal from the pore liquid, thus allowing analysis of the pore liquid relaxation without interference of the polymer signal.

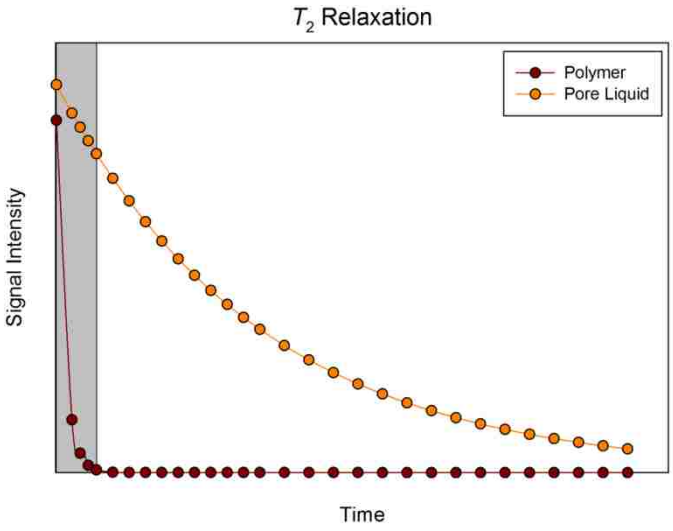

Figure 3.7. Comparison of polymer T_2 relaxation and pore liquid T_2 relaxation

4. RESULTS AND DISCUSSION

4.1. TRANSVERSE RELAXATION RESULTS

T_2-weighted relaxation profiles were obtained for isocyanate crosslinked base catalyzed aerogels (X-BC). At the top of Figure 4.1 there is a set of X-BC T_2-weighted relaxation profiles obtained at various relaxation delays. The left side of the profile is the signal from the acetone within the aerogel, and the right side of the profile is the signal from the bulk acetone. Corresponding points from each profile were fitted to an exponential decay to find the T_2 relaxation of acetone within the aerogel and within the bulk fluid. The bottom of Figure 4.1 is a plot of the T_2 relaxation time of acetone at points along the profile of the aerogel and bulk liquid. The relaxation time of the acetone signal within the aerogel was found to be 0.025 ± 0.001 s and the relaxation time of the bulk acetone signal was found to be 5.742 ± 0.006 s.

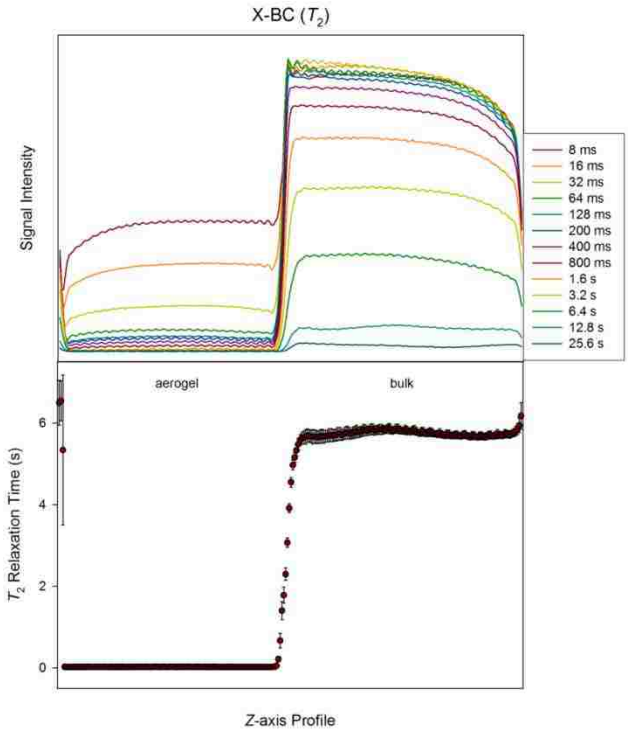

Figure 4.1. T_2-weighted relaxation profiles and the corresponding T_2 relaxation times of acetone within an isocyanate crosslinked base catalyzed silica aerogel and bulk acetone

Our goal was to compare the relaxation times within the aerogels to the pore sizes of the aerogels. However, the short relaxation time of the solvent signal within the aerogel leaves little room for variation in T_2 relaxation times. The small dynamic range of spin-spin relaxation time limits the usefulness of T_2 relaxation times for aerogel analysis. Therefore, T_2 relaxation times were not obtained for all of the aerogel samples.

4.2. LONGITUDINAL RELAXATION RESULTS

T_1-weighted relaxation profiles were obtained for all of the aerogel samples. The T_1-weighted profiles and corresponding T_1 relaxation times of acetone within a native base catalyzed silica aerogel (native BC) and bulk acetone can be seen in Figure 4.2.

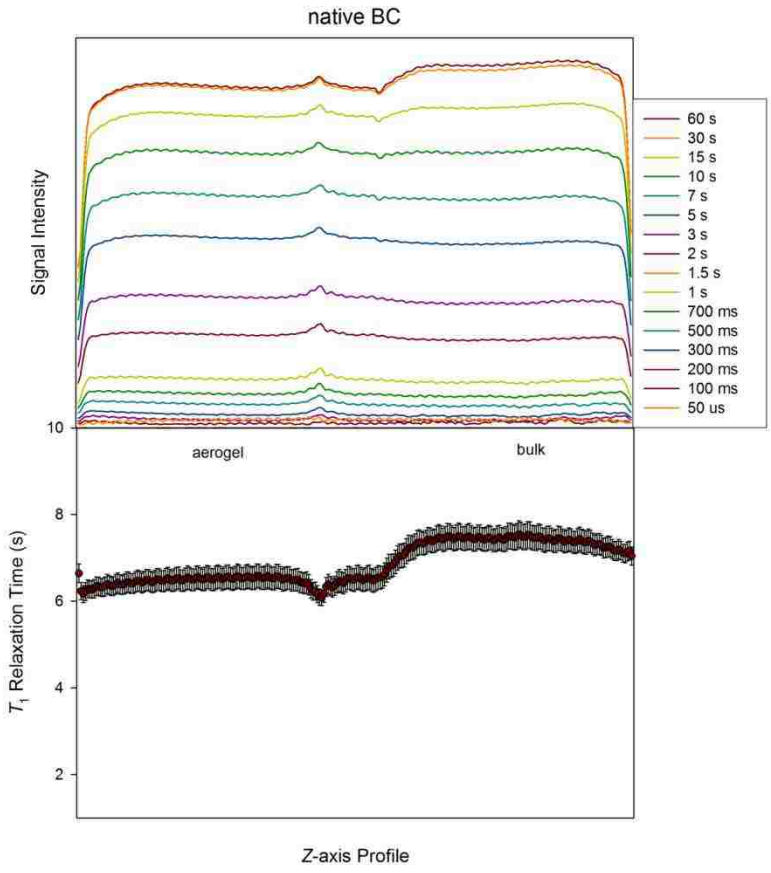

Figure 4.2. T_1-weighted relaxation profiles and the corresponding T_1 relaxation times of acetone within a native base catalyzed silica aerogel and bulk acetone

The initial signal intensity within the native base catalyzed aerogel and in the bulk is nearly equal due to the high porosity of the aerogel. The native silica aerogels are essentially porous glass, thus the pore surfaces were not expected to significantly enhance the relaxation time of the pore liquid. The relaxation time of the acetone signal within the aerogel was determined to be 6.34 ± 0.05 s and the relaxation time of the bulk acetone signal was determined to be 7.0 ± 0.1 s. The T_1 relaxation times of the pore liquid and the bulk liquid were reasonably close.

Figure 4.3 shows a set of T_1-weighted profiles and the corresponding T_1 relaxation times from an isocyanate crosslinked base catalyzed silica aerogel (X-BC).

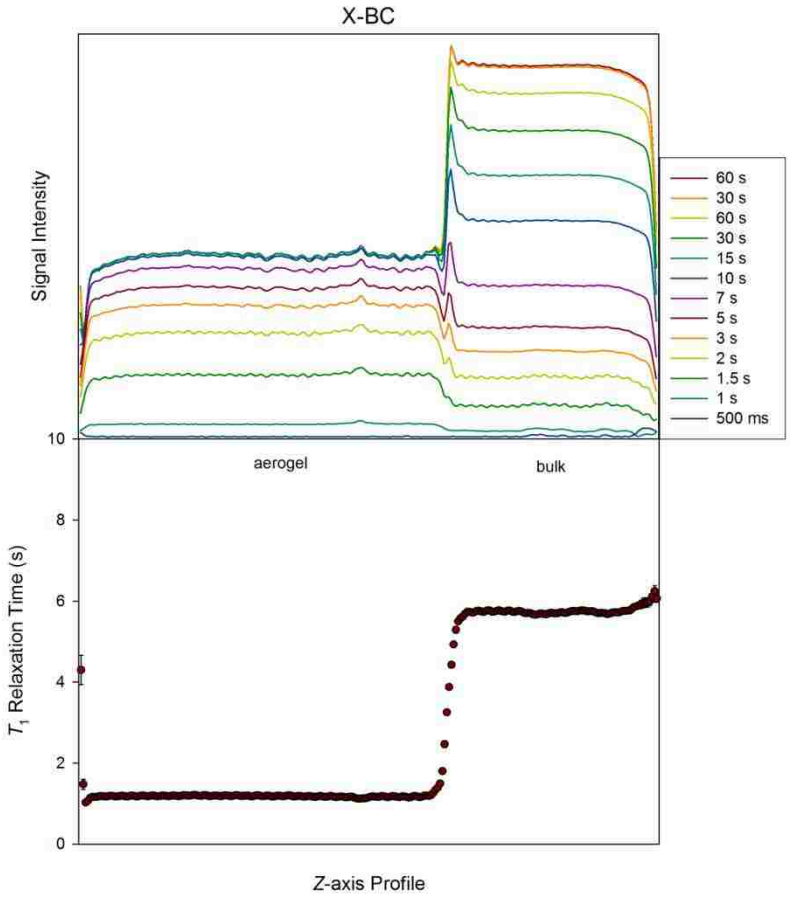

Figure 4.3. T_1-weighted relaxation profiles and the corresponding T_1 relaxation times of acetone within an isocyanate crosslinked base catalyzed silica aerogel and bulk acetone

The initial signal intensity within the isocyanate crosslinked base catalyzed aerogel is significantly lower than the signal intensity of the bulk; this is due to the additional space occupied by the crosslinking polymer. The relaxation time of the acetone signal within the aerogel was determined to be 1.18 ± 0.01 s and the relaxation time of the bulk acetone signal was determined to be 5.74 ± 0.01 s. The significant difference between the T_1 relaxation time of the pore liquid and the bulk liquid is largely due to the polymer crosslinking on the surface of the pores. The polymer layer causes an increase in the dipole-dipole interactions, resulting in a shorter T_1 relaxation time.

All of the isocyanate crosslinked silica aerogels were analyzed using the standard saturation-recovery pulse sequence with the gradient recalled echo imaging sequence. The aerogels crosslinked with methyl methacrylate (MMA) and styrene were found to have a significant amount of proton signal from the polymer. Figure 4.4 shows a set of T_1-weighted profiles and corresponding T_1 relaxation times for a silica aerogel crosslinked with 50 % MMA. The relaxation time of the acetone signal within the aerogel was found to be 1.53 ± 0.01 s and the relaxation time of the bulk acetone signal was found to be 6.51 ± 0.02 s. The fully relaxed profile shows a higher total signal within the aerogel than in the bulk solvent, indicating that more than just the solvent signal is being observed. If there was only solvent signal then there would be more signal in the bulk area, because the aerogel must take up some space reducing the amount of solvent in the region occupied by the aerogel.

Polymers generally have a very short relaxation time compared to small molecules. The short relaxation time can be selectively removed so that only the acetone relaxation is observed. An additional delay was added before the imaging sequence to allow time for the polymer to completely relax. After the delay time there is still sufficient remaining signal from the acetone to extract the relaxation time.

A set of T_1-weighted profiles and corresponding T_1 relaxation times for a silica aerogel crosslinked with 50 % MMA is shown in Figure 4.5. The T_1-weighted relaxation profiles in Figure 4.5 were collected using the modified pulse sequence including a delay to allow full relaxation of the polymer signal. As expected, the fully relaxed signal is greater for the bulk acetone than for the acetone within the aerogel. The relaxation time of the acetone signal within the aerogel was determined to be 3.87 ± 0.01 s and the

relaxation time of the bulk acetone signal was determined to be 6.30 ± 0.02 s. There is still a sufficient enhancement of the T_1 relaxation time of the pore liquid as compared to the bulk liquid. Relaxation time enhancement is expected due to the increased dipole-dipole interaction between the liquid and the pore surface. The relaxation enhancement within the MMA crosslinked aerogel is less than the enhancement within the isocyanate crosslinked aerogels. The decreased effect seems reasonable considering that the MMA crosslinking should be less polar than the isocyanate crosslinking. In addition, the isocyanate crosslinking is a stiffer crosslinking than the MMA crosslinkings. The less mobile isocyanate crosslinking should also enhance the relaxation time.

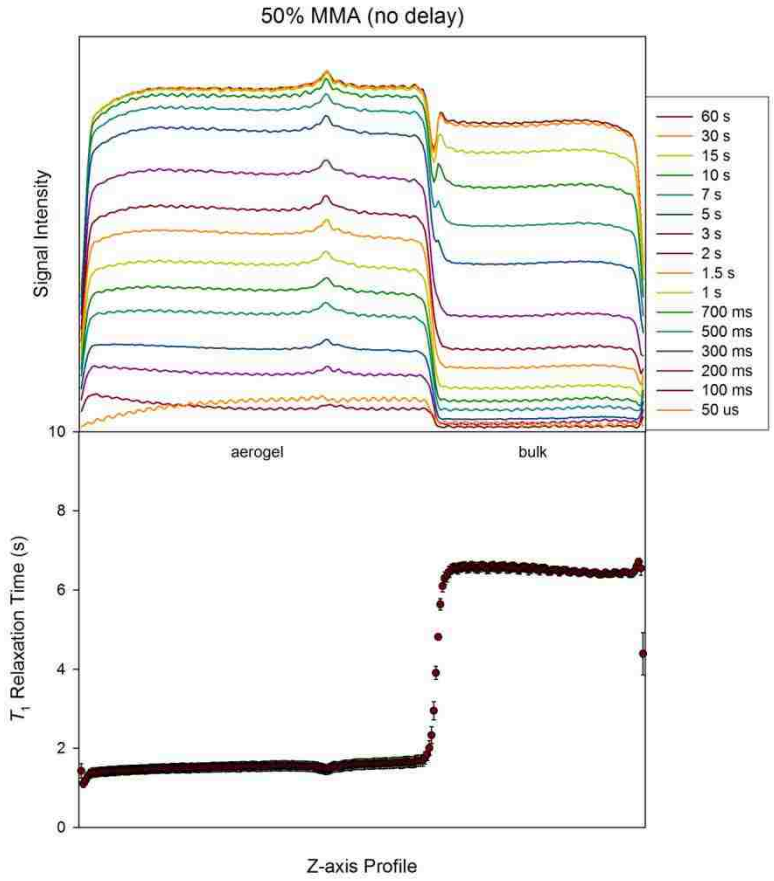

Figure 4.4. T_1-weighted relaxation profiles and the corresponding T_1 relaxation times of bulk acetone and acetone within a base catalyzed silica aerogel crosslinked with methyl methacrylate obtained without an additional delay for polymer relaxation

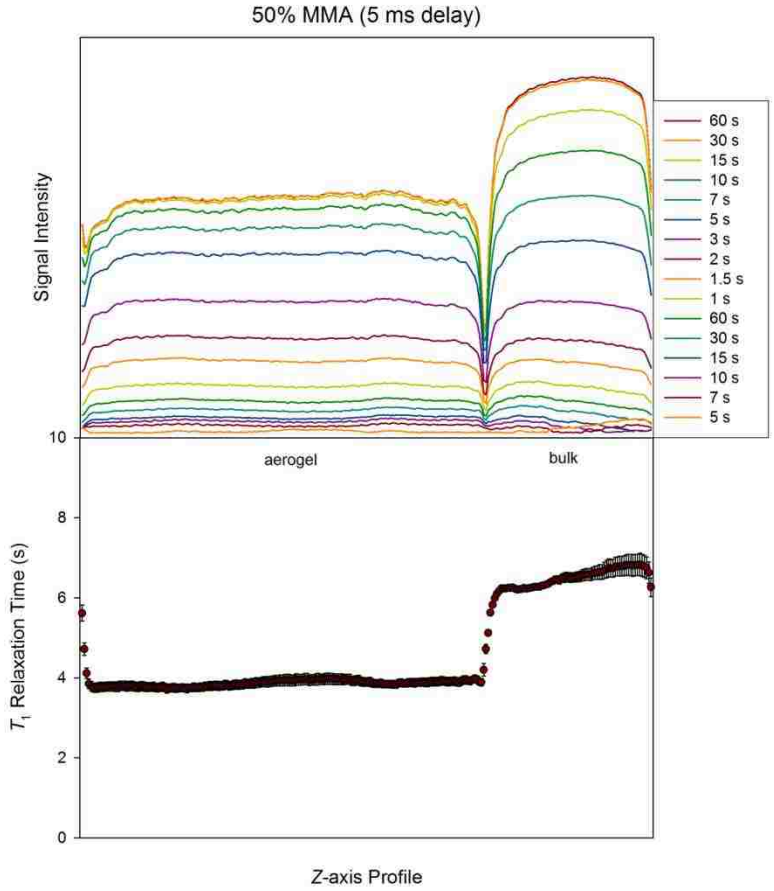

Figure 4.5. T_1-weighted relaxation profiles and the corresponding T_1 relaxation times of bulk acetone and acetone within a base catalyzed silica aerogel crosslinked with methyl methacrylate obtained with an additional 5 ms delay for polymer relaxation

Table 4.1 displays the T_1 relaxation times obtained for acetone contained in each aerogel and the bulk acetone above each aerogel. The bulk acetone relaxation times should remain constant, but as shown in Table 4.1 they vary from about 5.5 s to 7 s. Relaxation times can vary due to factors such as temperature and the calibration of radiofrequency pulses [6, 9].

The T_1 relaxation times given in Table 4.1 were normalized to account for variations and to obtain values that are valid for comparison between the samples. The T_1

relaxation times were normalized to a bulk acetone relaxation time of 6.25 s, the normalized T_1 relaxation times of the acetone within the aerogels are given in Table 4.2.

Table 4.1. T_1 relaxation times of bulk acetone and acetone within aerogel samples

Aerogel	Bulk Acetone Relaxation Time (s)	Pore Acetone Relaxation Time (s)
BC	7.0 ± 0.1	6.34 ± 0.05
X-BC	5.74 ± 0.01	1.18 ± 0.01
AC	6.38 ± 0.06	4.77 ± 0.07
X-AC	6.50 ± 0.01	1.17 ± 0.01
MP4	6.36 ± 0.01	2.26 ± 0.01
X-MP4	6.03 ± 0.01	1.08 ± 0.06
MP4-T045	6.56 ± 0.06	4.39 ± 0.03
X-MP4-T045	5.87 ± 0.04	1.01 ± 0.06
MP4-T065	6.25 ± 0.01	1.74 ± 0.01
X-MP4-T065	5.8 ± 0.1	0.90 ± 0.03
MP4-T200	5.52 ± 0.04	4.19 ± 0.01
MP4-T310	6.21 ± 0.01	2.82 ± 0.01
X-MP4-T310	6.68 ± 0.01	0.76 ± 0.01
Si-AIBN	6.2 ± 0.1	5.25 ± 0.06
50% MMA	6.30 ± 0.02	3.87 ± 0.01
50% styrene	6.09 ± 0.01	3.76 ± 0.01
75% styrene	6.50 ± 0.01	3.64 ± 0.01

The pore sizes and structure of the native base catalyzed aerogels, BC and Si-AIBN, are similar; both consist of a particulate structure with mesopores. The difference between the BC and Si-AIBN aerogels is the surface functionality. The BC aerogel has a hydroxyl surface functionality and the Si-AIBN aerogel has a bistriethoxysilane derivative of azobisisobutyronitrile (AIBN) incorporated on the surface. The AIBN

surface modification does not have a significant impact on the pore size or morphology of the aerogel, but it does increase the interaction of the pore liquid with the surface of the gel. This increase in surface interaction causes a slight decrease in the T_1 relaxation time due to the reduced mobility of the acetone.

Table 4.2. Normalized T_1 relaxation times of bulk acetone and acetone within aerogels

Aerogel	**Normalized Pore Liquid Relaxation Time (s)**
BC	5.67 ± 0.05
X-BC	1.28 ± 0.01
AC	4.68 ± 0.06
X-AC	1.13 ± 0.01
MP4	2.22 ± 0.01
X-MP4	1.12 ± 0.06
MP4-T045	4.20 ± 0.07
X-MP4-T045	1.08 ± 0.07
MP4-T065	1.74 ± 0.01
X-MP4-T065	0.97 ± 0.01
MP4-T200	4.76 ± 0.03
MP4-T310	2.84 ± 0.01
X-MP4-T310	0.71 ± 0.01
Si-AIBN	5.29 ± 0.06
50% MMA	3.84 ± 0.02
50% styrene	3.86 ± 0.01
75% styrene	3.50 ± 0.01

The native acid catalyzed aerogel (AC) has hydroxyl groups on the surface and a fibrous silica network with both mesopores and micropores. In addition to the relaxation enhancement due to the surface hydroxyl groups, the increased surface area due to the

micropores leads to a T_1 relaxation time that is shorter than both BC and Si-AIBN aerogels.

The T_1 relaxation times of the isocyanate crosslinked acid and base catalyzed aerogels, X-AC and X-BC, are significantly lower than the T_1 relaxation times of the native samples. The shortened relaxation time is due to the increased interaction of the pore liquid with the surface of the pores. Although the relaxation times of X-AC and X-BC are close, the change in the relaxation time of the base catalyzed sample was larger than that of the acid catalyzed sample. The native base catalyzed aerogels consists of a particulate structure with mesopores. The polymer crosslinking on the base catalyzed aerogel forms a layer onto the particulate structure and the mesoporous structure is retained. The acid catalyzed aerogel consists of a fibrous network with both mesopores and micropores. Polymer crosslinking on the acid catalyzed aerogels forms a coating on the fibers but fills the micropores in the process. The crosslinking results in significantly decreasing the available surface area for interaction in the acid catalyzed aerogel. The larger decrease in surface area for crosslinked acid catalyzed aerogels compared to the decrease in surface area for crosslinked base catalyzed aerogels results in a lower impact on the relaxation enhancement.

The aerogels crosslinked with methylmethacrylate and styrene all have shorter relaxation times than the native Si-AIBN aerogel from which they were prepared. The decreased relaxation time indicates an increased interaction of the pore liquid with the surface of the aerogel after crosslinking. In comparison to the T_1 relaxation time of the isocyanate crosslinked aerogels, the T_1 relaxation times of the MMA and styrene crosslinked aerogels is longer than for the isocyanate crosslinked aerogels. The main factor is likely the polarity difference between the polymers. The aerogels crosslinked with MMA and styrene are much less polar than the aerogels crosslinked with isocyanate. An additional factor that could affect the relaxation times is the flexibility of the crosslinking polymer. The isocyanate crosslinking is much more rigid than the MMA and styrene crosslinking. Relaxation times are related to the mobility of molecules, the less mobile a molecule is the shorter the relaxation time. Therefore, the pore liquid interacting with the less mobile isocyanate crosslinking should relax faster than the pore liquid interacting with the more mobile MMA and styrene crosslinking.

Considering the results of the acid and base catalyzed aerogels, native and isocyanate crosslinked, it is not a surprise that the T_1 relaxation time of all of the MP4 aerogels decreases significantly when crosslinked with isocyanate. All of the MP4 aerogels are prepared with a templating agent and with varying amounts of a swelling agent. The amounts of the templating and swelling agent for each aerogel can be found in Table 3.1. An increase in the amount of swelling agent seems to indicate that the pores would be larger and there would be less relaxation enhancement, but the amount of swelling agent is not strictly related to the pore size. The native MP4, MP4-T065, and MP4-T310 aerogels all have mesopores and macropores, whereas the native MP4-T045 and MP4-T200 aerogels only have macropores. Due to the combination of macropores and mesopores, the native MP4, MP4-T065, and MP4-T310 aerogels should have higher surface areas than the MP4-T045 and MP4-T200 aerogels which contain only macropores. Although the surface nature of all of the native MP4 aerogels should be comparable, the difference in available surface area for the pore liquid to interact is different. The higher available surface area of the MP4, MP4-T065, and MP4-T310 aerogels leads to shorter relaxation times than the MP4-T045 and MP4-T200 aerogels.

4.3. POROSITY

The porosity of an aerogel is generally calculated from the bulk and skeletal density of the gel, as shown in Equation 10. However, the porosity can also be determined from NMR intensities of the bulk fluid and pore fluid as shown in Equation 11. Table 4.3 lists the pore and bulk intensities for each gel and the porosities calculated from these measurements.

The porosities of the native base catalyzed aerogels, BC and Si-AIBN, are similar, both are highly mesoporous and the AIBN surface modification does not have an effect on the porosity. Although the native acid catalyzed aerogel, AC, contains micropores and mesopores, the overall porosity is comparable to the native base catalyzed aerogels. The porosity of the isocyanate crosslinked aerogels, X-AC and X-BC, are also comparable, although the porosities are reduced significantly compared to the native aerogels. The large change in porosity due to isocyanate crosslinking seems contrary to the explanation that crosslinking results in a thin conformal coating of polymer. However, the MMA and

styrene crosslinking seems to fit more reasonably to the thin conformal layer explanation, where the MMA and styrene crosslinked aerogels only have a reduction in porosity of about 15 % as opposed to the 45-50 % change in porosity after isocyanate crosslinking.

Table 4.3. Porosities calculated from NMR Intensities of pore fluid and bulk fluid

Aerogel	**Pore Fluid Intensity**	**Bulk Fluid Intensity**	**Porosity (%)**
BC	573,000 ± 1,000	621,000 ± 14,000	92.3
X-BC	470,000 ± 8,000	1,018,000 ± 7,000	46.2
AC	451,000 ± 9,000	485,000 ± 10,000	92.9
X-AC	454,000 ± 10,000	1,075,000 ± 9,000	42.3
MP4	318,000 ± 6,000	485,000 ± 3,000	65.6
X-MP4	339,000 ± 77,000	699,000 ± 190,000	48.5
MP4-T045	600,000 ± 29,000	650,000 ± 59,000	92.4
X-MP4-T045	264,000 ± 76,000	669,000 ± 210,000	39.4
MP4-T065	285,000 ± 12,000	473,000 ± 5,000	60.3
X-MP4-T065	341,000 ± 3,000	1,073,000 ± 12,000	31.8
MP4-T200	591,000 ± 25,000	611,000 ± 17,000	96.7
MP4-T310	344,000 ± 10,000	450,000 ± 6,000	76.3
X-MP4-T310	150,000 ± 12,000	455,000 ± 5,000	33.0
Si-AIBN	538,000 ± 25,000	569,000 ± 45,000	94.6
50% MMA	307,000 ± 53,000	377,000 ± 3,000	81.3
50% styrene	343,000 ± 28,000	428,000 ± 5,000	79.9
75% styrene	313,000 ± 68,000	401,000 ± 11,000	77.9

The native MP4-T045 and MP4-T200 aerogels are macroporous aerogels and have very high porosities. The MP4-T200 aerogel is prepared using more swelling agent, and does have a slightly higher porosity. The native MP4, MP4-T065, and MP4-T310 all have mesopores and macropores. The native MP4, MP4-T065, and MP4-T310 have

lower porosities than the templated gels with only macropores. However, as with the macroporous gels, an increase in the amount of swelling agent also increases the porosity. Similar to the native AC and BC, all of the templated aerogels have a significant decrease in porosity after crosslinking with isocyanate. Again, the significant change in porosity after crosslinking conflicts with the explanation that a thin conformal layer of polymer is added by crosslinking.

4.4. PORE SIZE

Pore size is related to the surface-to-volume ratio of a porous material. The surface areas of several of the aerogels were measured using nitrogen adsorption/ desorption using the BET method. BET surface areas were not available for the X-BC, MP4-T065, X-MP4-T065, and MP4-T200 aerogels. The surface area of a porous material along with the bulk density and porosity can be used to calculate the surface-to-volume ratio as shown in Equation 18. The surface-to-volume ratios of several of the aerogels were calculated and are listed in Table 4.4.

A pore shape must be assumed in order to relate the surface-to-volume ratio to a pore size. A spherical shape is often assumed and the pore radius is calculated. The pore size is generally of interest as related to the transport of fluids in porous media. The specific shape of the pore is not critical when studying the transport of fluid within porous media. The transport of fluid within porous media is instead generally related to the hydraulic radius of the porous media. The hydraulic radius is equal to the volume-to-surface ratio, or the inverse of the surface-to-volume ratio. The relationship between the hydraulic radius and the surface-to-volume ratio can be extracted from the combination of Equations 14 and 16. The hydraulic radius of each aerogel was determined from each surface-to-volume ratio and are shown in Table 4.5.

Although the hydraulic radii calculated for the native AC and BC fall into the macroporous range, the radii are relatively close to the expected mesoporous range. Also, the AC aerogel is smaller as expected considering the micropores that would reduce the average radius of the aerogel. The radius of the Si-AIBN aerogel is found to be significantly higher than the BC aerogel, although the radii of the Si-AIBN and BC aerogels are expected to be comparable. The radius of the X-AC aerogel is found to be

much smaller than the native AC aerogel. The X-AC aerogel is expected to retain its mesopores after crosslinking, but both the low porosity and the low hydraulic radius suggest otherwise.

Table 4.4. BET surface areas and surface-to-volume ratios
(*BET surface areas and bulk densities were measured by Sudhir Mulik)

Aerogel	**Bulk Density* (g/cm^3)**	**BET Surface Area* (m^2/g)**	**Surface-to-Volume Ratio (nm^{-1})**
BC	0.169 ± 0.004	997	0.0141
X-BC		-	-
AC	0.331 ± 0.008	714	0.0180
X-AC	0.522 ± 0.004	109	0.0778
MP4	0.299 ± 0.003	563	0.0882
X-MP4	0.755 ± 0.017	5.36	0.00430
MP4-T045	0.367 ± 0.003	612	0.0185
X-MP4-T045	0.663 ± 0.006	2.96	0.00301
MP4-T065		-	-
X-MP4-T065		-	-
MP4-T200		-	-
MP4-T310	0.189 ± 0.003	554	0.0324
X-MP4-T310	0.584 ± 0.003	1.31	0.00155
Si-AIBN	0.189 ± 0.005	973	0.0105
50% MMA	0.807 ± 0.047	46.05	0.00855
50% styrene	0.325 ± 0.008	183.4	0.0150
75% styrene	0.333 ± 0.014	160	0.0151

The native templated aerogels were all determined to have fairly small hydraulic radii. This is contrary to what is expected for macroporous materials. An even more problematic result is that the crosslinked templated samples all have very high calculated

radii, all significantly larger than their native counterparts. Similarly, the 50 % MMA and 75 % styrene aerogels also were found to have larger radii than their native counterpart. These results lead to the conclusion that the relaxation effects in the crosslinked samples are more complex than are being accounted for in our calculations.

Table 4.5. Hydraulic radii calculated from surface-to-volume ratios

Aerogel	**Hydraulic Radius (nm)**
BC	70.8
X-BC	-
AC	55.7
X-AC	12.9
MP4	11.3
X-MP4	232
MP4-T045	53.9
X-MP4-T045	332
MP4-T065	-
X-MP4-T065	-
MP4-T200	-
MP4-T310	30.8
X-MP4-T310	644
Si-AIBN	95.5
50% MMA	117
50% styrene	66.7
75% styrene	662

The surface-to-volume ratio and NMR relaxation times can also be used to determine the surface relaxivity parameter of porous media according to Equation 14. The surface relaxivity for each aerogel was calculated and are listed in Table 4.6.

Table 4.6. Surface relaxivities from surface-to-volume ratios

Aerogel	**Surface Relaxivity (nm/s)**
BC	1.17
X-BC	-
AC	2.99
X-AC	9.37
MP4	3.29
X-MP4	170
MP4-T045	4.22
X-MP4-T045	255
MP4-T065	-
X-MP4-T065	-
MP4-T200	-
MP4-T310	5.93
X-MP4-T310	804
Si-AIBN	2.78
50% MMA	11.8
50% styrene	6.63
75% styrene	8.30

The surface relaxivity is expected to be related to the nature of the surface. The native BC, AC, and Si-AIBN all have different surface functionality, so they are not easily compared. The surface of the native templated samples should be the same, but the calculated values of surface relaxivity are not very close to one another. The samples crosslinked with isocyanate also have very different calculated values of surface relaxivity. These results also indicate that there is something more complex than is being accounted for in our calculations. One possible problem with our calculations of surface-to-volume, hydraulic radius, and surface relaxivity could be due to the reliance on the specific surface area of the aerogels using nitrogen adsorption/desorption. Nitrogen can access pores down to 0.7 nm, but is only estimated to see pores smaller than 50 nm [27]. So this method may not be sufficient for the aerogels that are truly macroporous.

5. CONCLUSIONS

T_1- and T_2-weighted relaxation profiles of porous aerogels may be obtained by adding a one-dimensional NMR gradient-recalled echo imaging sequence to the end of standard T_1 and T_2 relaxation pulse sequences. The relaxation profiles can be used to determine the porosity of the aerogel in addition to extracting the T_1 and T_2 relaxation times of the fluid within the pores of the aerogel. T_1 relaxation times were found to relate to both the crosslinking polymer and the underlying aerogel structure.

T_2 relaxation times of the pore filling fluid were very short, on the order of milliseconds to tens of milliseconds. The short T_2 relaxation time is due to the fast diffusion of the fluid and the inhomogeneities in the magnetic field within the aerogel. The small dynamic range of T_2 relaxation times was not sufficient to yield information about the pore size and structure of the aerogels.

T_1 relaxation results from various native aerogels show a relationship between the aerogel structure and the T_1 relaxation time. Compared to the native base catalyzed aerogels, the native acid catalyzed aerogels are known to have a smaller average radius due to a significant amount of micropores. The native acid catalyzed aerogels were found to have shorter T_1 relaxation times than the native base catalyzed aerogels. The shortened relaxation time is attributed to the increased surface area, resulting in a larger fraction of fluid molecules interacting with the surface.

Surface interactions were shown to play a larger role in enhancing the relaxation time than the surface area of the aerogel. Polymer crosslinking reduces the surface area of the aerogel by filling in and blocking micropores and smoothing the surface of larger pores. The reduction in surface area reduces the number of fluid molecules that can interact with the pore surface. In general, the reduction of available surface leads to an increased mobility and a longer relaxation time. The opposite effect was observed for polymer crosslinked aerogels, the relaxation time was shortened after crosslinking. The reduced relaxation time is due to the increase in interaction between the fluid molecules and the polymer crosslinked surface. One factor that leads to increased interaction is larger dipole-dipole interactions between the polymer crosslinked surface and the fluid molecules. Another factor that will reduce the relaxation time is swelling of the polymer

crosslinking. Swelling of the polymer crosslinking can be thought of as increasing the available surface area for the fluid molecules to interact. The fluid within and near the polymer crosslinking will be hindered and have a short relaxation time, so there will be a larger fraction of molecules relaxing quickly as surface molecules.

Overall the T_1 relaxation times for the crosslinked aerogels were significantly shorter than the T_1 relaxation times for the native aerogels. The T_1 relaxation times were enhanced due to the increased interactions although the surface area of the crosslinked aerogels was decreased. There was also a difference in the extent of T_1 relaxation time enhancement relative to the crosslinking polymer. The isocyanate crosslinking lead to a significant decrease in the T_1 relaxation times, the relaxation times were reduced by a factor of about 4 for most aerogels crosslinked with isocyante. The T_1 relaxation times for the aerogels crosslinked with MMA and styrene were also shorter than the relaxation times of the native aerogels. The T_1 relaxation times from the isocyanate crosslinked aerogels were decreased more than the relaxation times from the MMA and styrene crosslinked aerogels. The increased enhancement is attributed to the more rigid and higher polarity of the isocyanate crosslinking in comparison with the MMA and styrene.

Unfortunately, relating NMR relaxation times to pore size will require an independent measurement of either surface area or surface relaxivity. Methods of measuring surface area of porous materials are generally limited to specific size ranges and would require the use of multiple techniques for one sample. The use of multiple techniques for one sample is inconvenient and time consuming. Surface relaxivity is also problematic. There are not tabulated values of surface relaxivities and there is not a simple method of measuring surface relaxivities. Surface relaxivities are specific to the pore surface in a given sample. The functionality, the thickness, and the extent of swelling are all elements that can affect the surface relaxivity.

6. FUTURE WORK

The results of this study show potential for using NMR as a tool to measure porosity and pore size of aerogels. There are concerns that will require further investigations.

The porosities were obtained after submerging the aerogels into acetone and allowing time for the fluid to penetrate the pores. The extent of pore filling was not confirmed and could have led to erroneous results for porosity. UV fluorescence and X-ray scattering experiments will be performed to check the extent of pore filling. In addition, after submerging the aerogels in fluid and allowing time for the fluid to penetrate, the samples will be put under vacuum to reduce the surface tension and capillary forces within the unfilled pores.

Results of the current study are inconclusive with respect to pore sizes. In order to relate the relaxation times with the pore sizes of the aerogels more experiments must be conducted. The results of the current study rely on surface areas measured using nitrogen adsorption/desorption using the BET method. The goal is to be able to use NMR as an independent tool to measure pore size. In order to use NMR independently for the measurement of pore sizes the surface relaxivity must be known. Measurement of surface relaxivity will require numerous additional experiments to study the interaction of fluids with various surfaces.

APPENDIX A.

T_1-WEIGHTED RELAXATION PROFILES AND T_1 RELAXATION TIMES

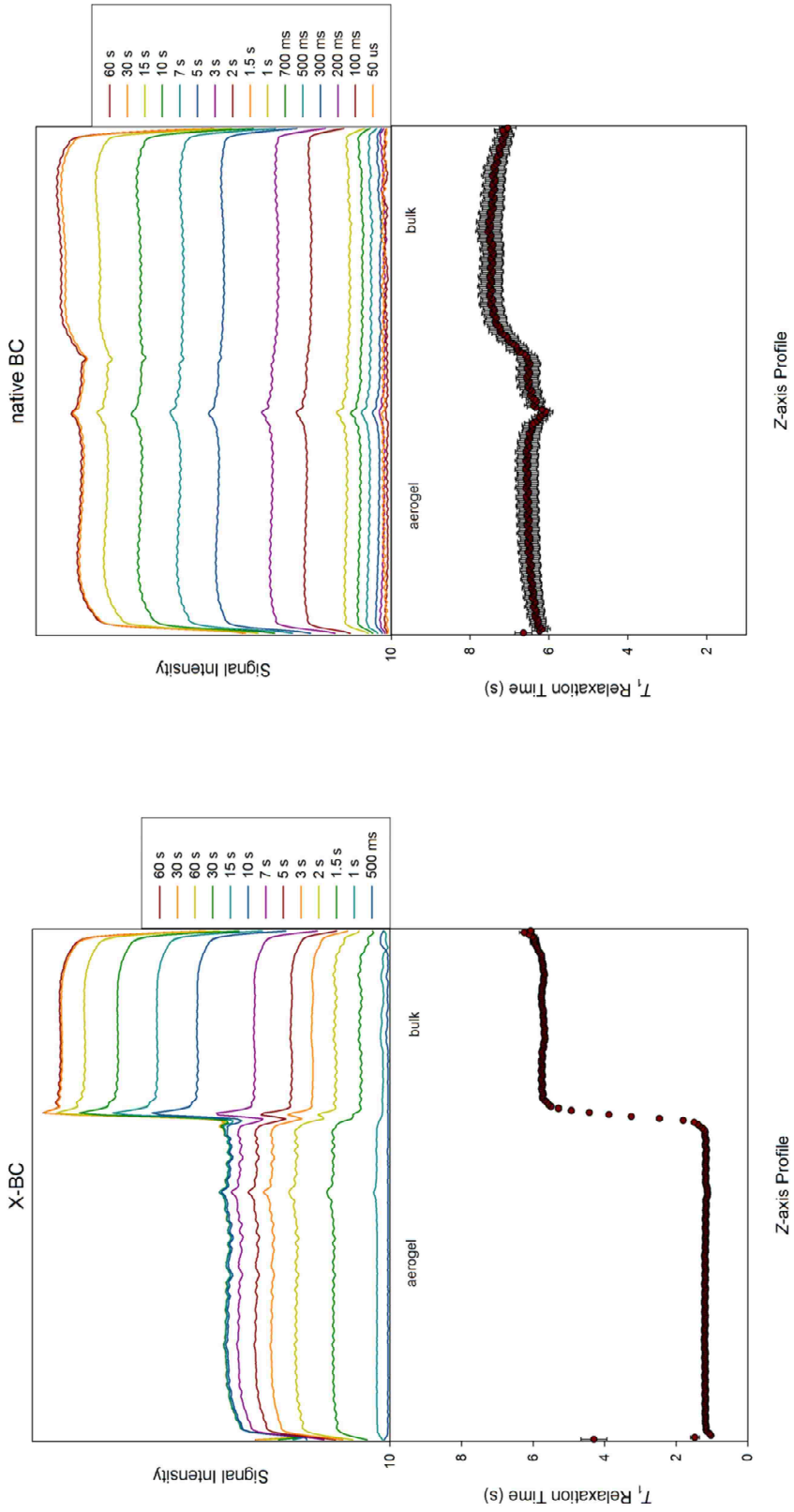
native BC
X-BC
Signal Intensity
T_1 Relaxation Time (s)
Z-axis Profile
aerogel
bulk
60 s
30 s
15 s
10 s
7 s
5 s
3 s
2 s
1.5 s
1 s
700 ms
500 ms
300 ms
200 ms
100 ms
50 us

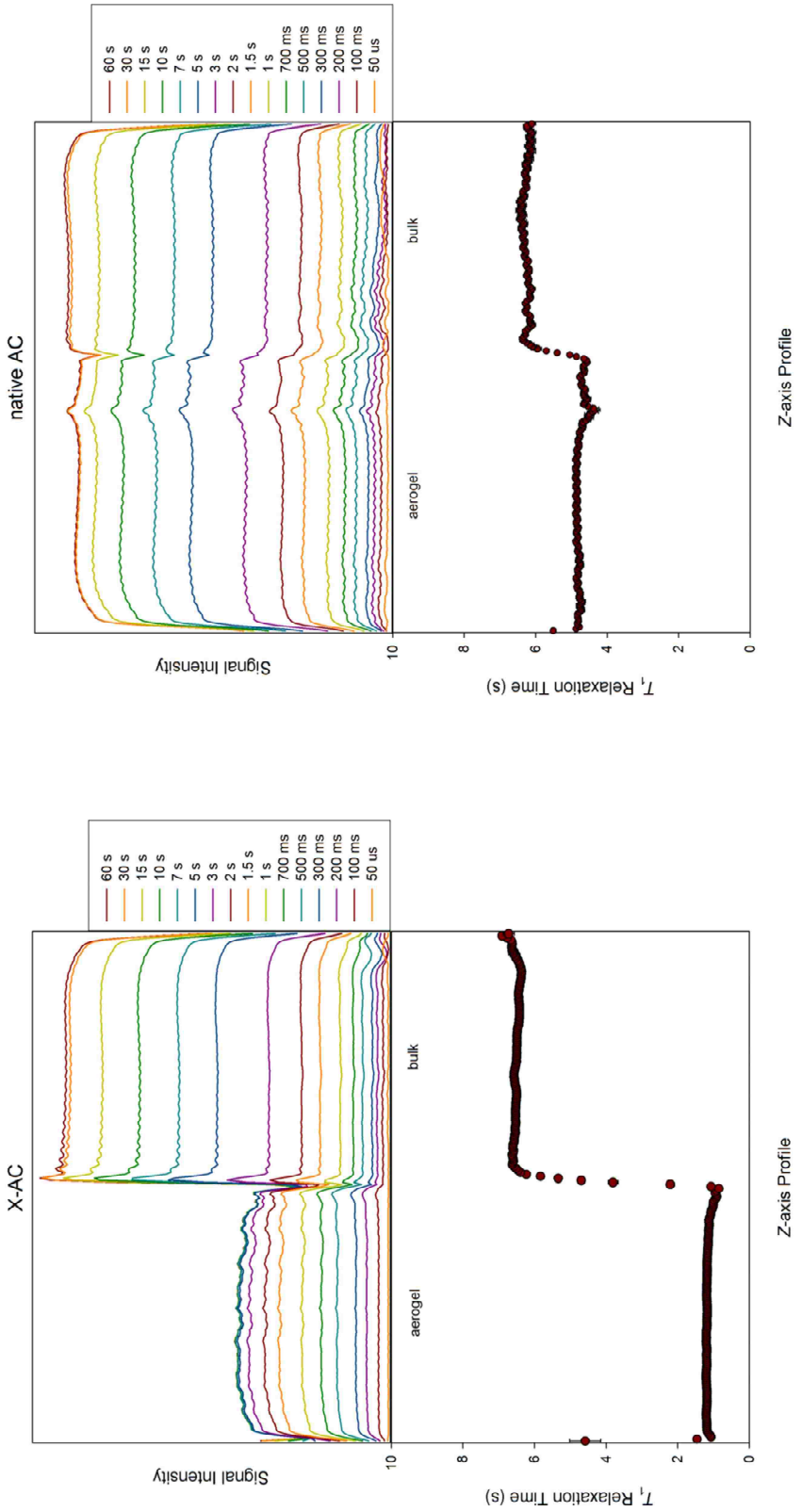
native AC
X-AC
Signal Intensity
60 s
30 s
15 s
10 s
7 s
5 s
3 s
2 s
1.5 s
1 s
700 ms
500 ms
300 ms
200 ms
100 ms
50 us
aerogel
bulk
T_1 Relaxation Time (s)
Z-axis Profile
0
2
4
6
8
10

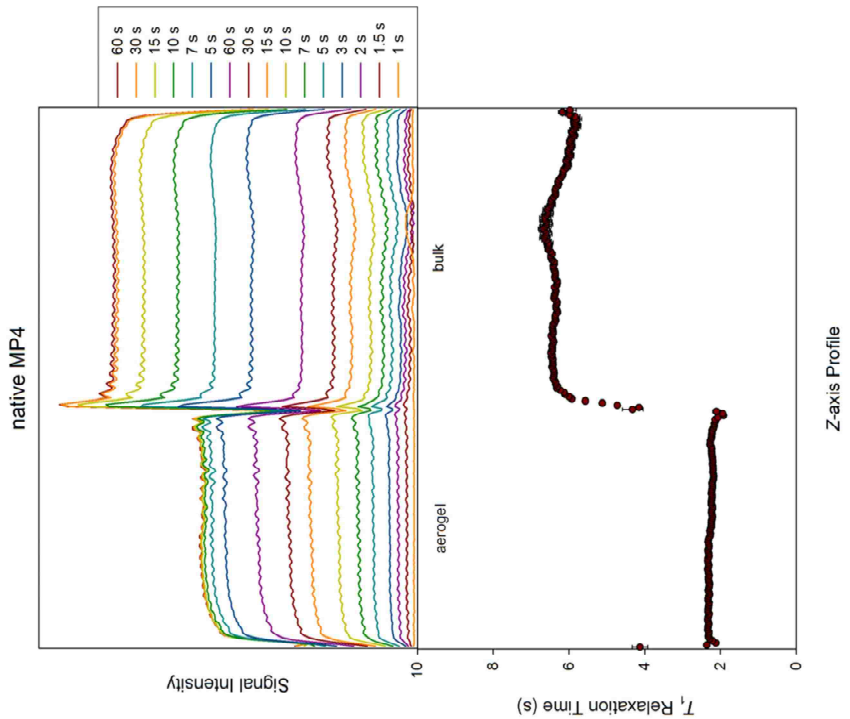
native MP4
Signal Intensity
60 s
30 s
15 s
10 s
7 s
5 s
60 s
30 s
15 s
10 s
7 s
5 s
3 s
2 s
1.5 s
1 s
aerogel
bulk
T_1 Relaxation Time (s)
Z-axis Profile

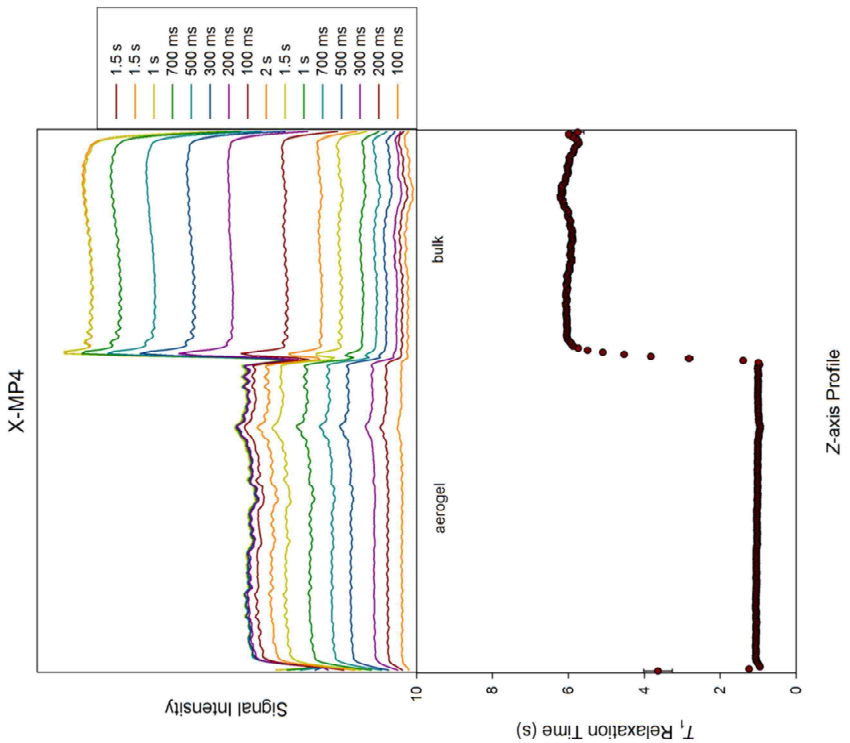
X-MP4
Signal Intensity
1.5 s
1.5 s
1 s
700 ms
500 ms
300 ms
200 ms
100 ms
2 s
1.5 s
1 s
700 ms
500 ms
300 ms
200 ms
100 ms
aerogel
bulk
T_1 Relaxation Time (s)
Z-axis Profile

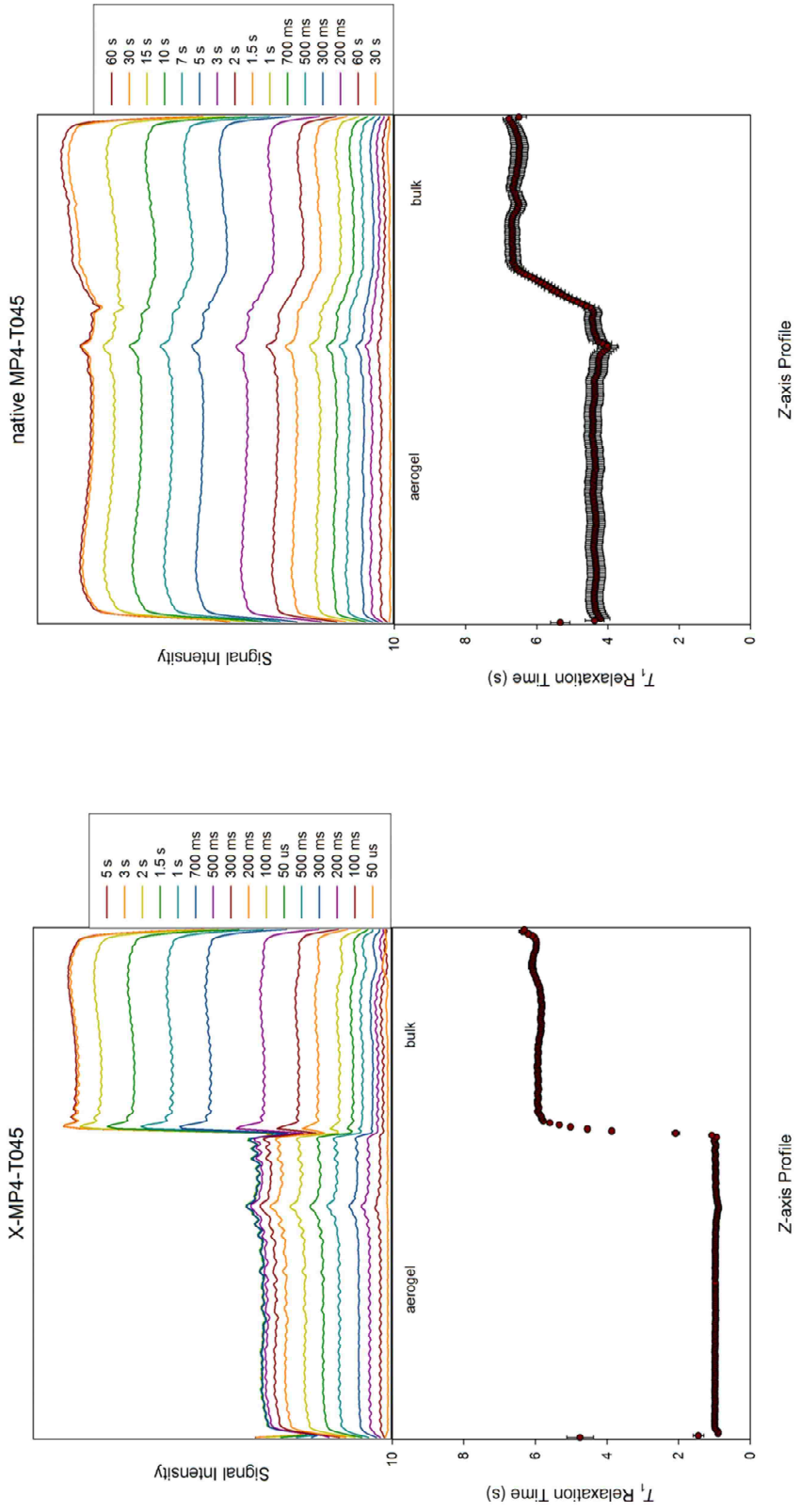
native MP4-T045
Signal Intensity
60 s
30 s
15 s
10 s
7 s
5 s
3 s
2 s
1.5 s
1 s
700 ms
500 ms
300 ms
200 ms
60 s
30 s
aerogel
bulk
T1 Relaxation Time (s)
Z-axis Profile
X-MP4-T045
Signal Intensity
5 s
3 s
2 s
1.5 s
1 s
700 ms
500 ms
300 ms
200 ms
100 ms
50 us
500 ms
300 ms
200 ms
100 ms
50 us
aerogel
bulk
T1 Relaxation Time (s)
Z-axis Profile

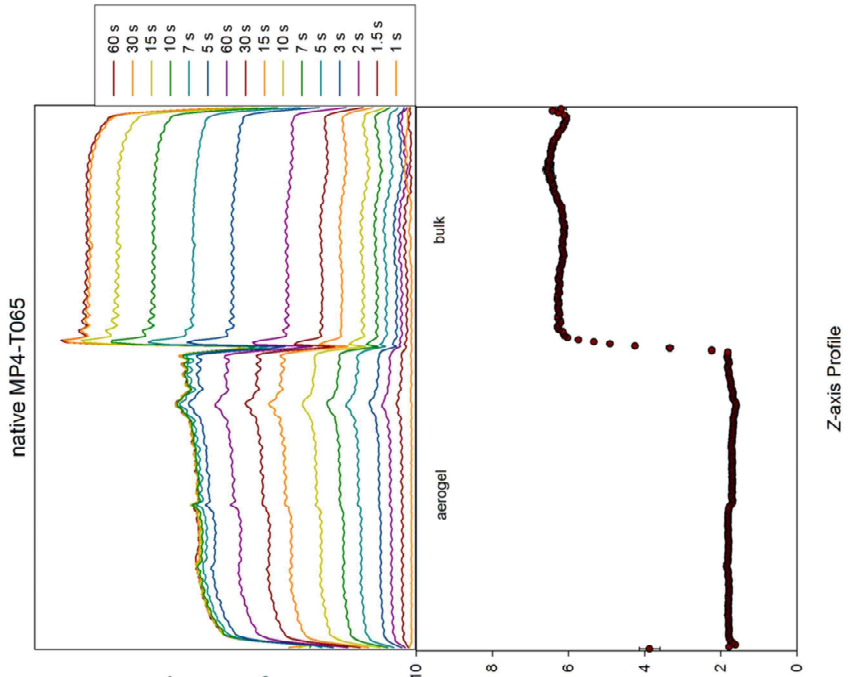
native MP4-T065
Signal Intensity
60 s
30 s
15 s
10 s
7 s
5 s
60 s
30 s
15 s
10 s
7 s
5 s
3 s
2 s
1.5 s
1 s
aerogel
bulk
T1 Relaxation Time (s)
Z-axis Profile

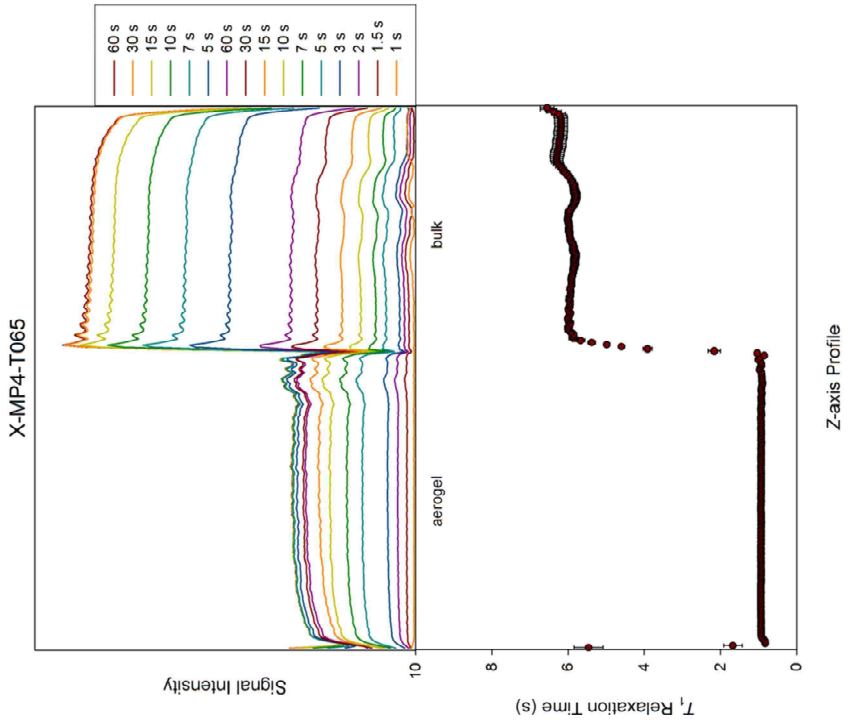
X-MP4-T065
Signal Intensity
60 s
30 s
15 s
10 s
7 s
5 s
60 s
30 s
15 s
10 s
7 s
5 s
3 s
2 s
1.5 s
1 s
aerogel
bulk
T1 Relaxation Time (s)
Z-axis Profile

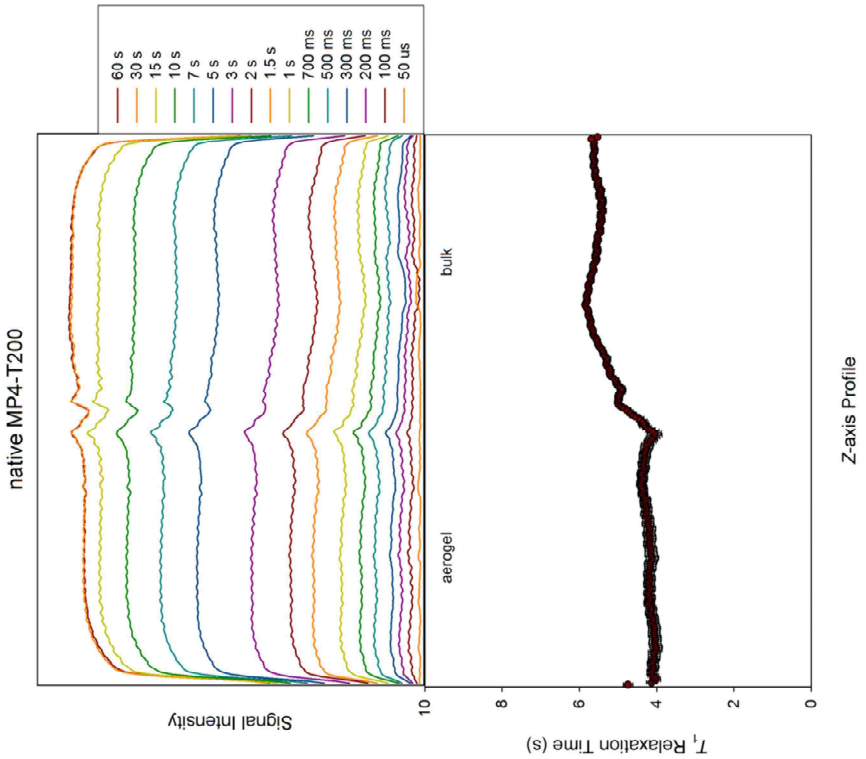
native MP4-T200
Signal Intensity
60 s
30 s
15 s
10 s
7 s
5 s
3 s
2 s
1.5 s
1 s
700 ms
500 ms
300 ms
200 ms
100 ms
50 us
aerogel
bulk
T1 Relaxation Time (s)
10
8
6
4
2
0
Z-axis Profile

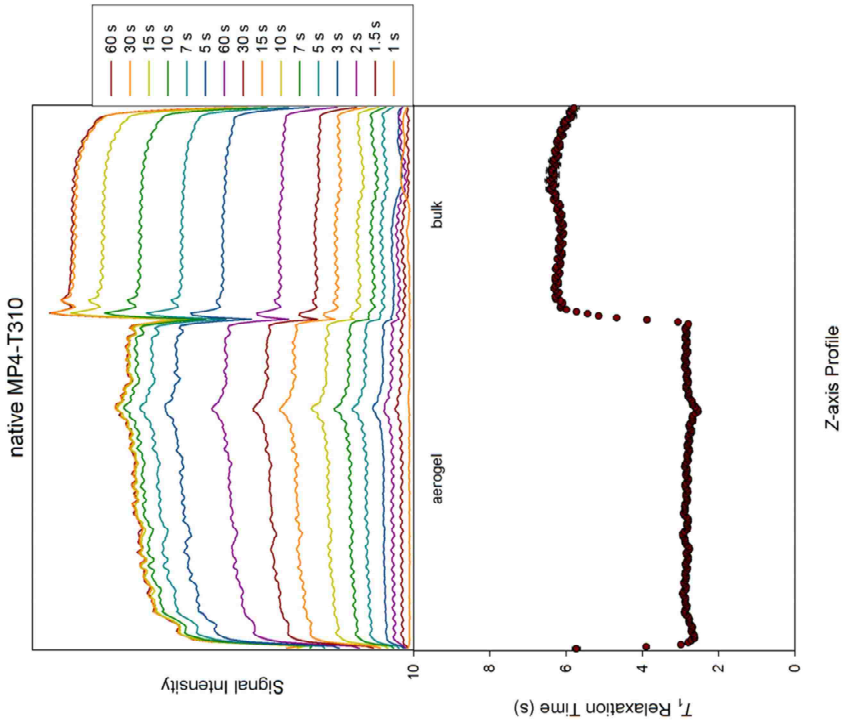
native MP4-T310
60 s
30 s
15 s
10 s
7 s
5 s
60 s
30 s
15 s
10 s
7 s
5 s
3 s
2 s
1.5 s
1 s
Signal Intensity
aerogel
bulk
T_1 Relaxation Time (s)
Z-axis Profile

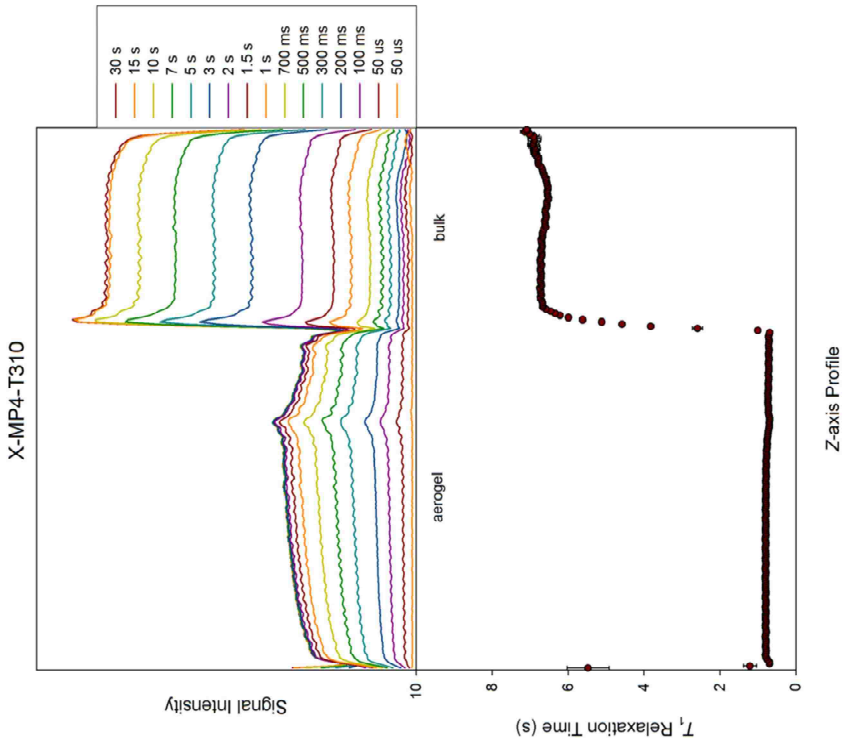
X-MP4-T310
30 s
15 s
10 s
7 s
5 s
3 s
2 s
1.5 s
1 s
700 ms
500 ms
300 ms
200 ms
100 ms
50 us
50 us
Signal Intensity
aerogel
bulk
T_1 Relaxation Time (s)
Z-axis Profile

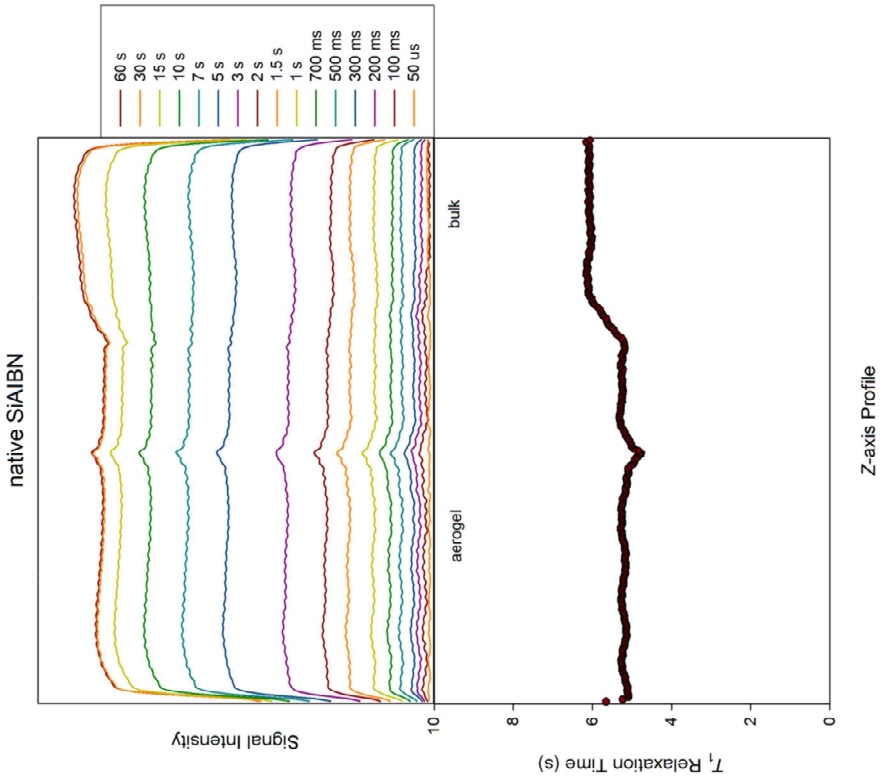
native SiAlBN
Signal Intensity
60 s
30 s
15 s
10 s
7 s
5 s
3 s
2 s
1.5 s
1 s
700 ms
500 ms
300 ms
200 ms
100 ms
50 us
aerogel
bulk
10
8
6
4
2
0
T1 Relaxation Time (s)
Z-axis Profile

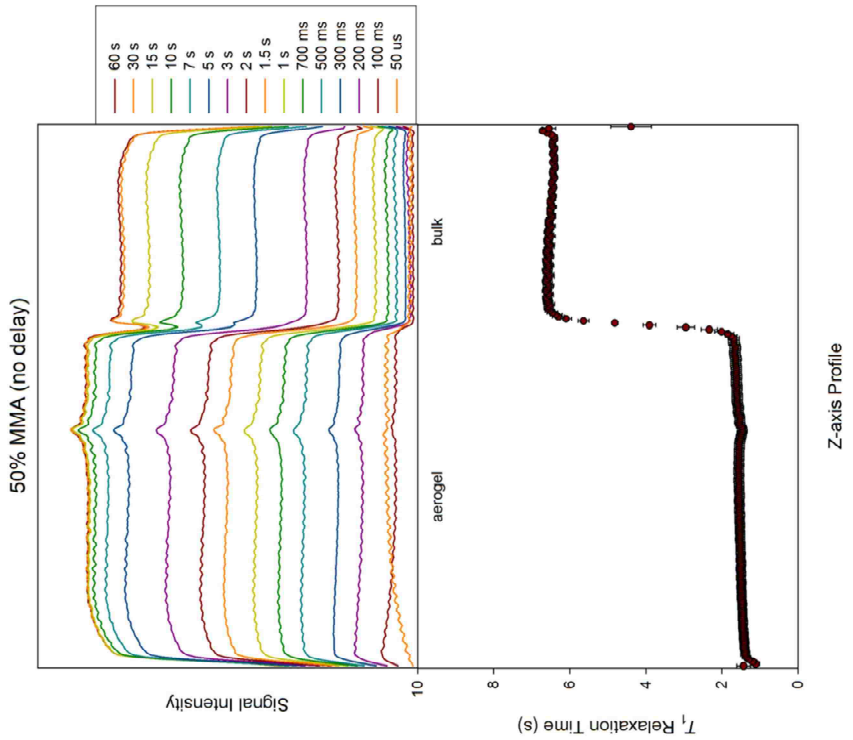
50% MMA (no delay)
Signal Intensity
60 s
30 s
15 s
10 s
7 s
5 s
3 s
2 s
1.5 s
1 s
700 ms
500 ms
300 ms
200 ms
100 ms
50 us
aerogel
bulk
T_1 Relaxation Time (s)
Z-axis Profile

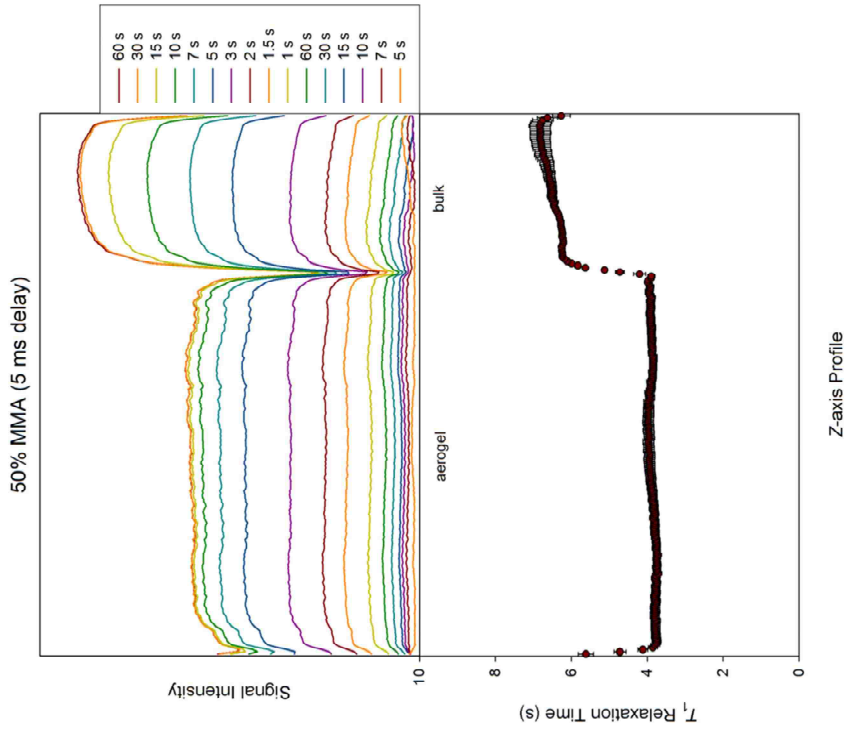
50% MMA (5 ms delay)
Signal Intensity
60 s
30 s
15 s
10 s
7 s
5 s
3 s
2 s
1.5 s
1 s
60 s
30 s
15 s
10 s
7 s
5 s
aerogel
bulk
T_1 Relaxation Time (s)
Z-axis Profile

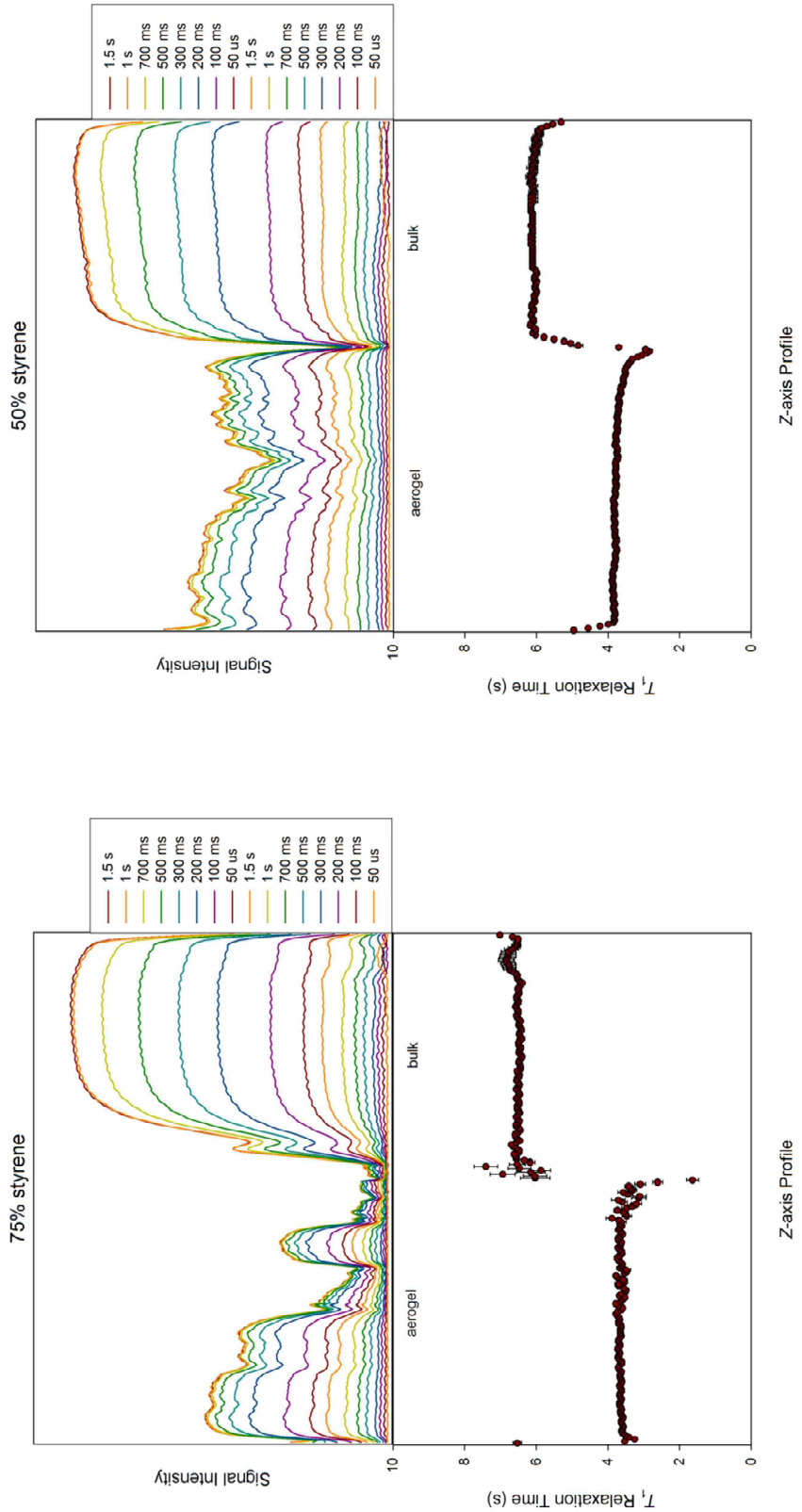
50% styrene
Signal Intensity
1.5 s
1 s
700 ms
500 ms
300 ms
200 ms
100 ms
50 us
1.5 s
1 s
700 ms
500 ms
300 ms
200 ms
100 ms
50 us
aerogel
bulk
T_1 Relaxation Time (s)
0
2
4
6
8
10
Z-axis Profile
75% styrene
Signal Intensity
aerogel
bulk
T_1 Relaxation Time (s)
Z-axis Profile

APPENDIX B.
PULSE PROGRAMS

ProfGradEchoT1

```
#include <Avance.incl>
#include <Grad.incl>
#include <De.incl>

"p2=p1*2"
"d11=30m"
"d28=d20-d27"
1 ze
  d11 UNBLKGRAD
2 d1
; --- inversion ---
  p2:f1 ph2
; --- recovery ---
  d19
  p1 ph1
  d20
; --- CPMG loop (n-2 pulses) ---
3 d20
  p2 ph2
  d20
; --- first gradient pulse ---
; --- and last CPMG pulse ---
  d27 gron1
  d28 groff
  p2 ph2
  d28
; --- profile acquisition ---
  d21 gron1
  ACQ_START
  aq DWELL_GEN
  5u groff
  rcyc=2
; --- write file and exit ---
  400m  wr #0
  d11 BLKGRAD
exit

ph1=0 0 2 2 1 1 3 3
ph2=1 3 1 3 0 2 0 2
ph30=0
ph31=0 0 2 2 1 1 3 3

;pl1 : f1 channel - power level for pulse (default)
;p1 : f1 channel -  90 degree high power pulse
;d1 : relaxation delay: 1-5 * T1
;d11 : delay for disk I/O [30 ms]
;d15 : variable echo time
;d21 : read grad. stab. delay [min. 250u)
;d27 : phase-encoding grad. length
;gpz1 : phase-encoding grad. amplitude
;gpz2 : read grad. amplitude
;NS: 1 or 2 * n
;DS: 0 or 4-8
```

ProfGradEchoT1MPT

```
#include <Avance.incl>
#include <Grad.incl>
#include <De.incl>

"p2=p1*2"
"d11=30m"
"d28=d20-d27"
1 ze
  d11 UNBLKGRAD
2 d1
; --- pulse train ---
4 vd
  p1:f1 ph3
  1u ivd
  lo to 4 times 11
; --- recovery time and 90 degree pulse ---
  d19
  p1 ph1
; --- first gradient pulse ---
  d27 gron1
  d28 groff
  p2 ph2
  d28
; --- profile acquisition ---
  d21 gron1
  ACQ_START
  aq DWELL_GEN
  5u groff
  rcyc=2
; --- write file and exit ---
  400m  wr #0
  d11 BLKGRAD
exit

ph1=0 0 0 0 0 0 0 0 2 2 2 2 2 2 2 2 1 1 1 1 1 1 1 1 3 3 3 3 3 3 3 3
ph2=1 1 1 1 3 3 3 3 1 1 1 1 3 3 3 3 0 0 0 0 2 2 2 2 0 0 0 0 2 2 2 2
ph3=0 2 1 3
ph30=0
ph31=0 0 0 0 0 0 0 0 2 2 2 2 2 2 2 2 1 1 1 1 1 1 1 1 3 3 3 3 3 3 3 3

;pl1 : f1 channel - power level for pulse (default)
;p1 : f1 channel -  90 degree high power pulse
;d1 : relaxation delay: 1-5 * T1
;d11 : delay for disk I/O [30 ms]
;d15 : variable echo time
;d21 : read grad. stab. delay [min. 250u)
;d27 : phase-encoding grad. length
;gpz1 : phase-encoding grad. amplitude
;gpz2 : read grad. amplitude
;NS: 1 or 2 * n
;DS: 0 or 4-8
```

ProfGradEchoT1MPTwdelay

```
#include <Avance.incl>
#include <Grad.incl>
#include <De.incl>

"p2=p1*2"
"d11=30m"
"d28=d20-d27"
1 ze
  d11 UNBLKGRAD
2 d1
; --- pulse train ---
4 vd
  p1:f1 ph3
  1u ivd
  lo to 4 times 11
; --- recovery time and 90 degree pulse ---
  d19
  p1 ph1
; --- T2 relaxation of polymer ---
d2
; --- first gradient pulse ---
  d27 gron1
  d28 groff
  p2 ph2
  d28
; --- profile acquisition ---
  d21 gron1
  ACQ_START
  aq DWELL_GEN
  5u groff
  rcyc=2
; --- write file and exit ---
  400m  wr #0
  d11 BLKGRAD
exit

ph1=0 0 0 0 0 0 0 0 2 2 2 2 2 2 2 2 1 1 1 1 1 1 1 1 3 3 3 3 3 3 3 3
ph2=1 1 1 1 3 3 3 3 1 1 1 1 3 3 3 3 0 0 0 0 2 2 2 2 0 0 0 0 2 2 2 2
ph3=0 2 1 3
ph30=0
ph31=0 0 0 0 0 0 0 0 2 2 2 2 2 2 2 2 1 1 1 1 1 1 1 1 3 3 3 3 3 3 3 3

;pl1 : f1 channel - power level for pulse (default)
;p1 : f1 channel -  90 degree high power pulse
;d1 : relaxation delay: 1-5 * T1
;d11 : delay for disk I/O [30 ms]
;d15 : variable echo time
;d21 : read grad. stab. delay [min. 250u)
;d27 : phase-encoding grad. length
;gpz1 : phase-encoding grad. amplitude
;gpz2 : read grad. amplitude
;NS: 1 or 2 * n
;DS: 0 or 4-8
```

ProfGradEchoT1PT

```
#include <Avance.incl>
#include <Grad.incl>
#include <De.incl>

"p2=p1*2"
"d11=30m"
"d28=d20-d27"
1 ze
  d11 UNBLKGRAD
2 d1
; --- pulse train ---
4 d17
  p1:f1 ph1
  lo to 4 times 100
; --- recovery time and 90 degree pulse ---
  d19
  p1 ph1
; --- first gradient pulse ---
  d27 gron1
  d28 groff
  p2 ph2
  d28
; --- profile acquisition ---
  d21 gron1
  ACQ_START
  aq DWELL_GEN
  5u groff
  rcyc=2
; --- write file and exit ---
  400m  wr #0
  d11 BLKGRAD
exit

ph1=0 0 2 2 1 1 3 3
ph2=1 3 1 3 0 2 0 2
ph30=0
ph31=0 0 2 2 1 1 3 3

;pl1 : f1 channel - power level for pulse (default)
;p1 : f1 channel -  90 degree high power pulse
;d1 : relaxation delay: 1-5 * T1
;d11 : delay for disk I/O [30 ms]
;d15 : variable echo time
;d21 : read grad. stab. delay [min. 250u)
;d27 : phase-encoding grad. length
;gpz1 : phase-encoding grad. amplitude
;gpz2 : read grad. amplitude
;NS: 1 or 2 * n
;DS: 0 or 4-8
```

ProfileGradEcho

```
#include <Avance.incl>
#include <Grad.incl>
#include <De.incl>

"d11=30m"
"p2=2*p1"
1 ze
  d11 UNBLKGRAD
2 d1
; --- preparation pulse ---
  p1:f1 ph1
; --- first gradient pulse ---
  d27 gron1
  5u groff
; --- evolution time ---
  d15
; --- profile acquisition ---
  d21 gron2
  ACQ_START
  aq DWELL_GEN
  5u groff
  rcyc=2
; --- write file and exit ---
  400m  wr #0
  d11 BLKGRAD
exit


ph1=0 0 2 2 1 1 3 3
ph2=1 3 3 1 2 0 0 2
ph30=0
ph31=0 0 2 2 1 1 3 3


;pl1 : f1 channel - power level for pulse (default)
;p1 : f1 channel -  90 degree high power pulse
;d1 : relaxation delay: 1-5 * T1
;d11 : delay for disk I/O [30 ms]
;d15 : variable echo time
;d21 : read grad. stab. delay [min. 250u)
;d27 : phase-encoding grad. length
;gpz1 : phase-encoding grad. amplitude
;gpz2 : read grad. amplitude
;NS: 1 or 2 * n
;DS: 0 or 4-8
```

ProfileGradEchoCPMG

```
#include <Avance.incl>
#include <Grad.incl>
#include <De.incl>

"p2=p1*2"
"d11=30m"
"d28=d20-d27"
"d19=d20-p2/3.1415"
1 ze
  d11 UNBLKGRAD
2 d1
; --- preparation pulse ---
  p1:f1 ph1
; --- first CPMG pulse with shortened first delay ---
; --- according to Huerliman, MRI 19 (2001) 375-378 ---
  d19
  p2 ph2
  d20
; --- CPMG loop (n-2 pulses) ---
3 d20
  p2 ph2
  d20
  lo to 3 times 2
; --- first gradient pulse ---
; --- and last CPMG pulse ---
  d27 gron1
  d28 groff
  p2 ph2
  d28
; --- profile acquisition ---
  d21 gron1
  ACQ_START
  aq DWELL_GEN
  5u groff
  rcyc=2
; --- write file and exit ---
  400m  wr #0
  d11 BLKGRAD
exit

ph1=0 0 2 2 1 1 3 3
ph2=1 3 1 3 0 2 0 2
ph30=0
ph31=0 0 2 2 1 1 3 3

;pl1 : f1 channel - power level for pulse (default)
;p1 : f1 channel -  90 degree high power pulse
;d1 : relaxation delay: 1-5 * T1
;d11 : delay for disk I/O [30 ms]
;d15 : variable echo time
;d21 : read grad. stab. delay [min. 250u)
;d27 : phase-encoding grad. length
;gpz1 : phase-encoding grad. amplitude      ;gpz2 : read grad. amplitude
;NS: 1 or 2 * n                             ;DS: 0 or 4-8
```

ProfileGradEchoPFG

```
#include <Avance.incl>
#include <Grad.incl>
#include <De.incl>

"p2=p1*2"
"d11=30m"
"d28=d20-d27"
"d19=d20-p2/3.1415"
1 ze
  d11 UNBLKGRAD
2 d1
; --- preparation pulse ---
  p1:f1 ph1
; --- first gradient pulse ---
; --- and last CPMG pulse ---
  d27 gron1
  d28 groff
  p2 ph2
  d20
  d20
  p2 ph2
  d20
  d20
  p2 ph2
  d28
; --- profile acquisition ---
  d21 gron1
  ACQ_START
  aq DWELL_GEN
  5u groff
  rcyc=2
; --- write file and exit ---
  400m  wr #0
  d11 BLKGRAD
exit

ph1=0 0 2 2 1 1 3 3
ph2=1 3 1 3 0 2 0 2
ph30=0
ph31=0 0 2 2 1 1 3 3

;pl1 : f1 channel - power level for pulse (default)
;p1 : f1 channel -  90 degree high power pulse
;d1 : relaxation delay: 1-5 * T1
;d11 : delay for disk I/O [30 ms]
;d15 : variable echo time
;d21 : read grad. stab. delay [min. 250u)
;d27 : phase-encoding grad. length
;gpz1 : phase-encoding grad. amplitude
;gpz2 : read grad. amplitude
;NS: 1 or 2 * n
;DS: 0 or 4-8
```

zgdelayed

```
;zg
;avance-version (00/02/07)
;1D sequence


#include <Avance.incl>


1 ze
2 d1
  p1 ph1
  d2
  go=2 ph31
  wr #0
exit

ph1=0 2 2 0 1 3 3 1
ph31=0 2 2 0 1 3 3 1



;pl1 : f1 channel - power level for pulse (default)
;p1 : f1 channel -  high power pulse
;d1 : relaxation delay; 1-5 * T1



;$Id: zg,v 1.6 2000/05/08 11:41:13 eng Exp $
```

BIBLIOGRAPHY

[1] Friebolin, Horst. Basic One- and Two-Dimensional NMR Spectroscopy. New York, NY: Wiley-VCH, 2005.

[2] Harris, Robin K. "Nuclear Spin Properties & Notation." Encyclopedia of Nuclear Magnetic Resonance. Ed. David M. Grant, Robin K. Harris. New York: John Wiley, 2002

[3] Gerstein, B.C. "Rudimentary NMR: The Classical Picture." Encyclopedia of Nuclear Magnetic Resonance. Ed. David M. Grant, Robin K. Harris. New York: John Wiley, 2002

[4] Levitt, Malcolm H. Spin Dynamics. Chicester: Wiley-Blackwell, 2001.

[5] Traficante, D.D. "Relaxation: An Introduction." Encyclopedia of Nuclear Magnetic Resonance. Ed. David M. Grant, Robin K. Harris. New York: John Wiley, 2002

[6] Howarth, O.W. "Recording One-Dimensional High Resolution Spectra." Encyclopedia of Nuclear Magnetic Resonance. Ed. David M. Grant, Robin K. Harris. New York: John Wiley, 2002

[7] Bain, A.D. "Radiofrequency Pulses: Response of Nuclear Spins." Encyclopedia of Nuclear Magnetic Resonance. Ed. David M. Grant, Robin K. Harris. New York: John Wiley, 2002

[8] Hill, H.D.W. "Specctrometers: A General Overview." Encyclopedia of Nuclear Magnetic Resonance. Ed. David M. Grant, Robin K. Harris. New York: John Wiley, 2002

[9] Bakhmutov, Vladimir I. Practical NMR Relaxation for Chemists. Hoboken, NJ: Wiley, 2004.

[10] Avent, A.G. "Spin Echo Spectroscopy of Liquid Samples." Encyclopedia of Nuclear Magnetic Resonance. Ed. David M. Grant, Robin K. Harris. New York: John Wiley, 2002

[11] Phalippou, J., et al. "Aerogel Processing." Handbook of Sol-Gel Science and Technology. Ed. Hiromitsu Kozuka. Boston: Kluwer Academic Publishers, 2004

[12] Gesser, H.D. and P.C. Goswami. “Aerogels and Related Porous Materials.” Chem. Rev. 89 (1989): 765-788.

[13] Sakka, Sumio. “The Outline of Applications of the Sol-Gel Method.” Handbook of Sol-Gel Science and Technology. Ed. Sumio Sakka. Boston: Kluwer Academic Publishers, 2004

[14] Husing, N. and U. Schubert. “Aerogels – Airy Materials: Chemistry, Structure, and Properties.” Angew. Chem. Int. Ed. 37 (1998): 22-45.

[15] Jones, S.M. “Aerogel: Space Exploration Applications.” Journal of Sol-Gel Science and Technology. 40 (2006): 351-357.

[16] Pajonk, G.M. “Some Applications of Silica Aerogels.” Colloid Polym Sci. 281 (2003): 637-651.

[17] Dorcheh, A.S. and M.H. Abbasi. “Silica Aerogel; Synthesis, Properties and Characterization.” Journal of Materials Processing Technology. 199 (2008): 10-26.

[18] Zhang, G., et al. “Isocyanate-crosslinked Silica Aerogel Monoliths: Preparation and Characterization.” Journal of Non-Crystalline Solids. 350 (2004): 152-164.

[19] Leventis, N., et al. “Nanoengineering Strong Silica Aerogels.” Nano Letters. 2.9 (2002): 957-960.

[20] Leventis, N., et al. “Polymer Nano-Encapsulation of Templated Mesoporous Silica Monoliths with Improved Mechanical Properties.” Journal of Non-Crystalline Solids. 354 (2008): 632-644.

[21] Gurav, J.L., et al. “Silica Aerogel: Synthesis and Applications.” Journal of Nanomaterials. 2010 (2010): 1-11.

[22] Katti, A., et al. “Chemical, Physical, and Mechanical Characterization of Isocyanate Cross-Linked Amine-Modified Silica Aerogels.” Chem. Mater. 18 (2006): 285-296.

[23] Meador, M.B., et al. “Cross-Linking Amine-Modified Silica Aerogels with Epoxies: Mechanically Strong Lightweight Porous Materials.” Chem. Mater. 17 (2005): 1085-1098.

[24] Ilhan, E.F., et al. “Hydrophobic Monolithic Aerogels by Nanocasting Polystyrene on Amine-Modified Silica.” Journal of Materials Chemistry. 16 (2006): 3046-3054.

[25] Mulik, S., et al. “Crosslinking 3D Assemblies of Nanoparticles into Mechanically Strong Aerogels by Surface-Initiated Free Radical Polymerization.” Chem. Mater. 20 (2008): 5035-5046.

[26] Leventis, N., A. Palczer, and L. McCorkle. “Nanoengineering Silica-Polymer Composite Aerogels with No Need for Supercritical Fluid Drying.” Journal of Sol-Gel Science and Technology. 35 (2005): 99-105.

[27] Nakanishi, K. “Porosity Measurement.” Handbook of Sol-Gel Science and Technology. Ed. Rui M. Almeida. Boston: Kluwer Academic Publishers, 2004

[28] Gallegos, D.P., et al. “A NMR Technique for the Analysis of Pore Structure: Application to Materials with Well-Defined Pore Structure.” Journal of Colloid and Interface Science. 119.1 (1987): 127-140.

[29] Hua, D.W., et al. “Structural analysis of silica aerogels.” Journal of Non-Crystalline Solids. 186 (1995): 142-148.

[30] Barrie, P.J. “Characterization of Porous Media Using NMR Methods.” Annual Reports on NMR Spectroscopy. Ed. G.A. Webb. New York: Academic Press, 2000

[31] Viola, R., et al. “NMR techniques: A non-destructive analysis to follow microstructural changes induced in ceramics.” Journal of the European Ceramic Society. 26 (2006): 3343-3349.

[32] Junker, F. and W.S. Veeman. “Time-dependent xenon diffusion measurements in microporous silicon imidonitrides by pulsed field gradient NMR spectroscopy.” Chemical Physics Letters. 305 (1999): 39-43.

[33] Gallegos, D.P., D.M. Smith, and C.J. Brinker. “An NMR Technique for the Analysis of Pore Structure: Application to Mesopores and Micropores.” Journal of Colloid and Interface Science. 124 (1988): 186-198.

[34] D'Orazio, F., et al. "Application of nuclear magnetic resonance pore structure analysis to porous silica glass." Journal of Applied Physics. 65 (1989): 742-751.

[35] Bryar, T.R. and R.J. Knight. "Laboratory studies of the effect of sorbed oil on proton nuclear magnetic resonance." Geophysics. 68 (2003): 942-948.

[36] Mitra, P.P. and P.N. Sen. "Effects of microgeometry and surface relaxation on NMR pulsed-field-gradient experiments: Simple pore geometries." Physical Review B. 45 (1992): 143-156.

[37] Borgia, G.C., R.J.S. Brown, and P. Fantazzini. "Nuclear magnetic resonance relaxivity and surface-to-volume ratio in porous media with a wide distribution of pore sizes." Journal of Applied Physics. 79 (1996): 3656-3664.

[38] Liaw, H., et al. "Characterization of Fluid Distributions in Porous Media by NMR Techniques." AlChE Journal. 42.2 (1996): 538-546.

[39] Crooks, L.E. "Image Formation Methods." Encyclopedia of Nuclear Magnetic Resonance. Ed. David M. Grant, Robin K. Harris. New York: John Wiley, 2002

[40] Canet, D. "Radiofrequency Gradient Pulses." Encyclopedia of Nuclear Magnetic Resonance. Ed. David M. Grant, Robin K. Harris. New York: John Wiley, 2002

VITA

EmmaLou Theresa Satterfield was born in Kansas City, Missouri on August 5, 1982. In May 2005, she received her B.S. degree cum laude in Chemistry from the University of Missouri-Rolla, now Missouri University of Science and Technology. She entered graduate school at Missouri S&T and performed research in the field of NMR under the direction of Dr. Klaus Woelk. She presented preliminary findings of this research in March 2008 at the 49th national Experimental NMR Conference (ENC). She received her M.S. degree in Chemistry in December 2011.